Lithos 388–389 (2021) 106069

Contents lists available at ScienceDirect

Lithos

journal homepage: www.elsevier.com/locate/lithos

Research Article

High-Mg andesitic rocks formed through crustal magmatic differentiation

Yang Yu [a,b], Xiao-Long Huang [a,b,*], Min Sun [c], Peng-Li He [a,b], Chao Yuan [a,b]

[a] State Key Laboratory of Isotope Geochemistry, Guangzhou Institute of Geochemistry, Chinese Academy of Sciences, Guangzhou 510640, China
[b] CAS Center for Excellence in Deep Earth Science, Guangzhou 510640, China
[c] Department of Earth Sciences, The University of Hong Kong, Pokfulam Road, Hong Kong

ARTICLE INFO

Article history:
Received 2 October 2020
Received in revised form 19 February 2021
Accepted 19 February 2021
Available online 25 February 2021

Keywords:
High-Mg andesitic rocks
Fractional crystallization
High Ba and Sr
Low Sr/Y
Wuyi-Yunkai Orogen
South China

ABSTRACT

High-Mg andesitic rocks are enriched in both compatible (Mg, Cr and Ni) and incompatible elements (Si, Ba and Sr), which indicates the complexity of their petrogenesis. Models involving hybridization of the mantle sources and input of adakitic melts have been invoked, but struggle to explain the low Mg# values (<0.65) of some low Sr/Y (<40) high-Mg andesitic rocks, because these rocks cannot represent primary melts (Mg# ≥ 0.72) produced by the partial melting of mantle peridotite. This study presents a petrological and geochemical analysis of the Xinsi diorite (443 ± 3 Ma) and Tiechang gabbro (440 ± 3 Ma) from the Early Paleozoic Wuyi-Yunkai Orogen in South China, and demonstrates the role of magmatic differentiation in the petrogenesis of high-Mg andesitic rocks. These rocks contain high SiO_2, MgO, Ba and Sr concentrations with low Mg# values (≤0.69) and Sr/Y ratios (≤16.7), resembling typical low Sr/Y high-Mg andesitic rocks. Amphiboles and clinopyroxenes in the Xinsi diorite contain variable contents of Ba and Sr, both of which negatively correlate with Mg#. This indicates that their parental melts had low Ba and Sr and underwent significant enrichment of Ba and Sr through the fractionation of Mg-rich minerals within upper crust (3.1–4.4 kbar). Clinopyroxene, plagioclase and biotite in the Tiechang gabbro all contain lower Ba and Sr than those in the Xinsi diorite, suggesting that their parental melts were also initially low in Sr and Ba and experienced enrichment of these elements during magma evolution at middle crustal levels (5.7–6.3 kbar). The low Ba and Sr concentrations and Sr/Y ratios for parental melts of the Xinsi diorite and Tiechang gabbro suggest their derivation from the partial melting of mantle sources with input from slab melts at shallow depths without involvement of abundant garnet in petrogenesis. This study demonstrates the importance of fractional crystallization in the genesis of low Sr/Y high-Mg andesitic rocks and is conflict with past views that their geochemical features were related to the involvement of adakitic melts in their mantle sources. Therefore, this study presents an alternative model for the production of low Sr/Y and high Sr/Y high-Mg andesitic rocks, particularly in the Late Archean, which reflects the intense melting of subducted slab at different depths in the hotter mantle regime at that time.

1. Introduction

High-Mg andesites have attracted great interest because of their striking similarities with bulk crust (Martin et al., 2010; Shirey and Hanson, 1984; Tatsumi, 2006; Tatsumi and Ishizaka, 1982). In addition, high-Mg andesitic rocks occurred at 3.0–2.5 Ga in most cratons, implying a correlation between their occurrence and initiation of modern style subduction (Laurent et al., 2014; Nebel et al., 2018; Shirey and Hanson, 1984; Smithies et al., 2004, 2005, 2019; Smithies and Champion, 2000; Stern et al., 1989; Tatsumi and Ishizaka, 1982). Deciphering the petrogenesis of high-Mg andesite is important for understanding the formation of the continental crust, and may also further our understanding of the origin and evolution of subduction-zone tectonic on Earth.

High-Mg andesitic rocks occur mainly from the Late Archean to the Cenozoic and possess similar geochemical characteristics, such as high SiO_2 (55–60 wt%) and high Mg# (>0.60) and unusual enrichments of both compatible elements (e.g., Ni and Cr) and incompatible elements (e.g., Sr and Ba; Kay, 1978; Martin et al., 2010; Shirey and Hanson, 1984; Smithies and Champion, 2000; Smithies et al., 2004, 2005; Stern et al., 1989; Tatsumi, 2006). Their high MgO, Cr and Ni contents lead to a general consensus that high-Mg andesitic magmas were formed through mantle processes, but it remains unclear how these rocks acquire their crust-like enrichments in K, Ba, Sr, and light rare earth elements (LREE). The concentrations of these elements vary considerably among high-Mg andesitic rocks, such as those in the Late Archean

* Corresponding author at: State Key Laboratory of Isotope Geochemistry, Guangzhou Institute of Geochemistry, Chinese Academy of Sciences, Guangzhou 510640, China.
E-mail address: xlhuang@gig.ac.cn (X.-L. Huang).

https://doi.org/10.1016/j.lithos.2021.106069
0024-4937/

(e.g., Sr = 143–2502 ppm and Ba = 316–4407 ppm; Martin et al., 2010). This compositional variability is mainly attributed to different petrogenetic processes in the mantle, including different metasomatic interactions (Martin et al., 2005, 2010; Rapp et al., 1999, 2010; Smithies and Champion, 2000), and/or variable compositions among the metasomatic agents (Heilimo et al., 2010; Lobach-Zhuchenko et al., 2008; Steenfelt et al., 2005; Stern et al., 1989).

It is notable that many high-Mg andesitic rocks, particularly those in the Late Archean, have Mg# values of <0.65 (Martin et al., 2010), which is much lower than those of melts derived from the partial melting of peridotite metasomatized by trondhjemite-tonalite-diorite (TTG) melts (Mg# = 0.76–0.77; Rapp et al., 2010) or primary magmas (Mg# > 0.75) from hot ambient mantle during the Late Archean (Herzberg et al., 2010). Therefore, these high-Mg andesitic rocks cannot be primary melts in equilibrium with mantle peridotite, and must have undergone extensive magmatic differentiation. In contrast, some studies suggest that magmatic differentiation plays an insignificant role in the petrogenesis of high-Mg andesitic rocks because the K_2O, Ba and Sr concentrations in these rocks poorly correlate with SiO_2 (Laurent et al., 2014 and references therein). However, whole-rock geochemical compositions can be also influenced by several magmatic processes, such as crustal assimilation and crystal accumulation, in addition to fractional crystallization. Thus, poor correlations between incompatible elements and SiO_2 cannot exclude a role for magmatic differentiation in the petrogenesis of high-Mg andesite. Recent experimental research indicates that high-Mg basaltic melts can undergo ~40–60% crystallization at 1100–1200 °C and generate residual melts with Mg# values of 0.58–0.64 (Ulmer et al., 2018). The relatively low Mg# values of many high-Mg andesitic rocks suggests that they may represent residual melts after extensive fractionation of Mg-rich minerals, such as clinopyroxene, orthopyroxene and olivine. Because K, Ba and Sr are all strongly incompatible in these Mg-rich minerals (Adam and Green, 2006; Beattie, 1994; Hart and Dunn, 1993), their high abundance in the high-Mg andesitic rocks might be partially attributed to magmatic differentiation. Therefore, while untested, fractional crystallization may play an important role in the petrogenesis of high-Mg andesite.

The Early Paleozoic Wuyi-Yunkai orogeny was the first extensive tectonic event after the formation of the South China Block by the amalgamation of the Yangtze and Cathaysia blocks during the Early Neoproterozoic (e.g., Li et al., 2006). This orogen was developed in the inner South China Block and is bounded by the Anhua-Luocheng Fault to the west and the Zhenghe-Dapu Fault to the east (Fig. 1), and is, therefore, interpreted as an intracontinental orogenic belt (Li et al., 2010; Yu et al., 2018). However, this orogen differs from other typical intracontinental orogens, such as the Early Paleozoic Alice Spring Orogeny in Australia. Large amounts of felsic rocks and minor mafic rocks were produced in the Wuyi-Yunkai Orogen, suggesting intense mantle-crust interactions (Yu et al., 2018). Some andesitic rocks in the Wuyi-Yunkai Orogen contain high concentrations of MgO, Ba and Sr (Liu et al., 2018; Yu et al., 2018), compositionally resembling typical high-Mg andesite. These high MgO-Ba-Sr andesitic rocks have Mg# values of <0.70 and are thought to have formed due to the Early Paleozoic subduction of the Huanan Ocean beneath the Cathaysia Block. The Wuyi-Yunkai Orogen is thus interpreted as a collisional, rather than an intracontinental, orogenic belt (Liu et al., 2018). Therefore, deciphering the petrogenesis of the high-Mg andesitic rocks is crucial for understanding the tectonic evolution of the Wuyi-Yunkai Orogen.

Unlike whole-rock geochemistry, the trace element signature of mineral is dominantly controlled by the composition of the melts from which these minerals crystallize, according to the Rayleigh fractionation law (Hermann et al., 2001). In situ analysis of the major and trace element of minerals can characterize the chemical evolution of magma

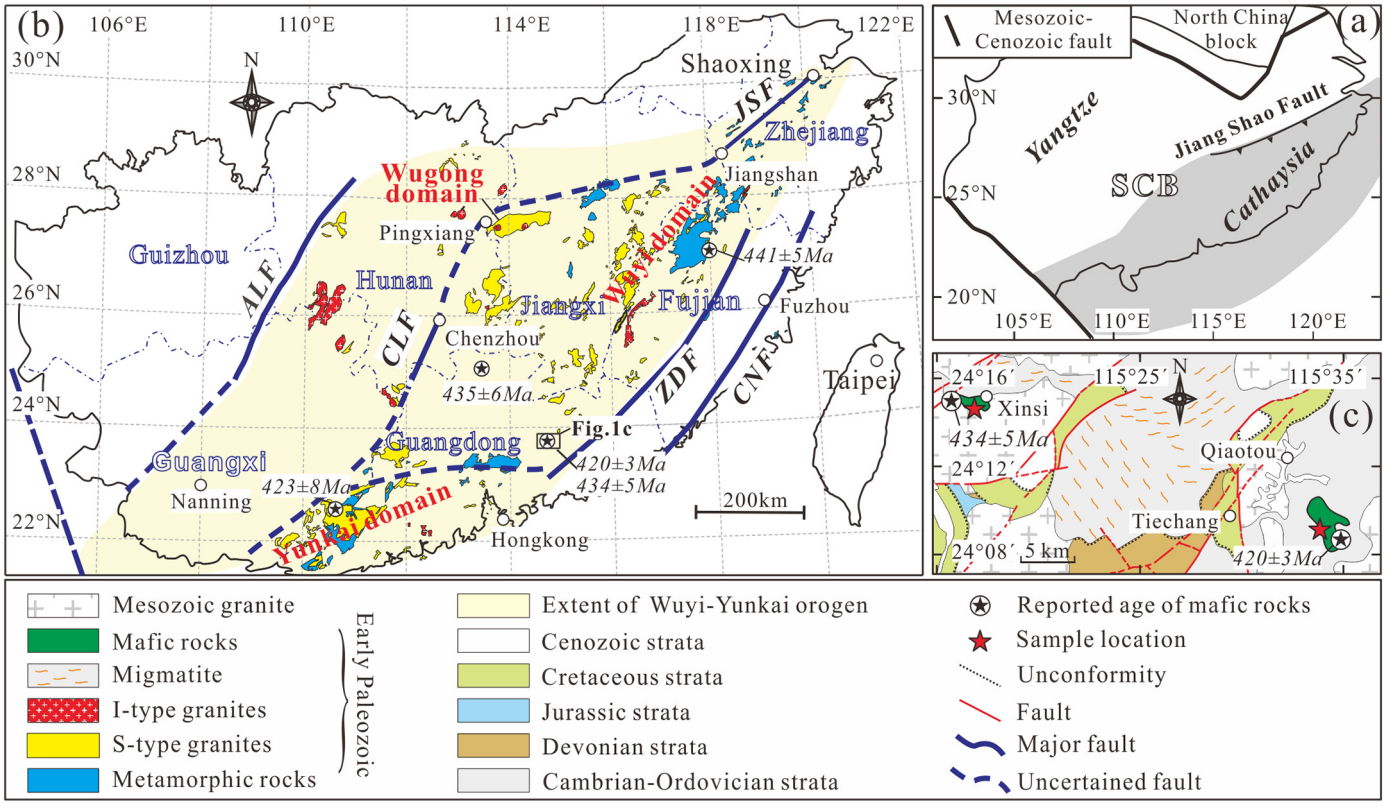

Fig. 1. (a) Map of the South China Block showing the outline of the Yangtze and Cathaysia blocks (modified from Li et al., 2010); (b) map of the eastern South China Block, showing the known extent of the Early Paleozoic Wuyi-Yunkai Orogen (modified from Li et al., 2010; Wang et al., 2013; Yu et al., 2018); and (c) simplified geological map showing the sample locations of the Xinsi diorite and Tiechang gabbro. Geochronology data of mafic rocks are from Wang et al. (2013). Abbreviations are as follows: ALF = Anhua-Luocheng Fault; JSF = Jiangshan-Shaoxing Fault; CLF = Chenzhou-Linwu Fault; ZDF = Zhenghe-Dapu Fault; CNF = Gaoyao-Huilai Fault.

chambers (e.g. Qian and Hermann, 2010). In this study, two groups of high-Mg andesitic rocks were collected from the Xinsi high-Mg diorite and Tiechang biotite-bearing gabbro in the Wuyi-Yunkai Orogen (Fig. 1). Whole-rock major and trace elements, whole-rock Sr—Nd isotopes, in situ major and trace element abundances of minerals, and zircon U—Pb age and Hf—O isotopes are presented, in order to discuss the magma sources and magma evolution processes involved in producing these rocks. A process for generating the high-Mg andesitic melts mainly by magmatic differentiation of mantle-derived melts at different crustal levels is proposed, which offers new perspectives on the petrogenesis of high-Mg andesite, including those that formed during the Late Archean.

2. Geological background and sample petrography

2.1. Geological background

The South China Block consists of the Yangtze Block in the northwest and the Cathaysia Block in the southeast (Fig. 1a). The Early Paleozoic Wuyi-Yunkai orogeny resulted in large-scale magmatism and the development of a widespread unconformity between the Devonian and Early Paleozoic sedimentary sequences in the eastern South China Block (Yu et al., 2018). The Early Paleozoic magmatism comprised predominantly peraluminous S-type granites with minor I-type granite and mafic rocks (e.g., Huang et al., 2013; Wang et al., 2011; Yu et al., 2016, 2018). The S-type granites are exposed over an area of >20,000 km^2 in the eastern Yangtze and western Cathaysia blocks (Fig. 1b), while I-type granites and mafic rocks are mainly distributed near the tectonic boundary (Fig. 1b). This suggests the emplacement of mantle-derived magmas along a weakened lithospheric zone (Yu et al., 2018). Both mafic and felsic rocks in the orogen show negative whole-rock $\varepsilon_{Nd}(t)$ and zircon $\varepsilon_{Hf}(t)$ values, excluding significant input of juvenile materials from the asthenosphere mantle (Wang et al., 2013).

2.2. Sample petrography

Samples were collected from the Xinsi diorite and Tiechang gabbro in northern Guangdong Province, South China (Fig. 1b), which intrude Cambrian-Ordovician strata and are overlain by Devonian strata (Fig. 1c). Some Early Paleozoic amphibole gabbros (420–434 Ma) also outcrop in the area (Wang et al., 2013; Fig. 1c). However, it is difficult to clarify the relationship between the studied intrusions and the reported amphibole gabbro in the field due to their poor exposure. The Xinsi diorite is composed of clinopyroxene (Cpx, 1–5%), amphibole (Am, 35–40%), biotite (Bt, 15–20%), plagioclase (Pl, 25–30%), K-feldspar (Kfs, 5–10%) and quartz (Qtz, 5–10%; Fig. 2a-d) with accessory magnetite, zircon, apatite, monazite and titanite (Fig. 2). Clinopyroxenes are elliptical and skeletal crystals with green amphibole rims (Fig. 2a, b and d). There are two types of amphiboles in the studied samples. First, some anhedral amphiboles (A02–1; Fig. 2a and b) occur as the core of clinopyroxene (C02–1), with both being replaced by the green amphibole on their rims (A02–2; Fig. 2a and b). Second, some amphiboles (A02–3; Fig. 2c) show normal zonation with brown cores and green rims. Plagioclase is euhedral or subhedral, while biotite, quartz and K-feldspar are mainly present as interstitial phases between other minerals.

The Tiechang gabbro contains clinopyroxene (35–40%), orthopyroxene (5–10%), biotite (10–15%), plagioclase (25–30%), K-feldspar (5–10%) and quartz (5–10%) (Fig. 2e-h) with accessory zircon, apatite, monazite and magnetite (Fig. 2e). Clinopyroxenes are subhedral and contain abundant inclusions of orthopyroxene, plagioclase, biotite and magnetite (Fig. 2f and g). Orthopyoxenes and biotites are subhedral crystals (Fig. 2f-h). The plagioclases are subhedral and occasionally show well-developed normal zonation (Fig. 2h). Quartz and K-feldspar are generally present as interstitial phases between other minerals.

3. Analytical methods

The analyses in this study were all conducted at the State Key Laboratory of Isotope Geochemistry (SKLaBIG), Guangzhou Institute of Geochemistry, Chinese Academy of Sciences (GIG-CAS). Detailed analytical procedures and conditions are similar to those described by Yu et al. (2018).

Two big samples (>5 kg) from the Xinsi diorite and Tiechang gabbro were selected for zircon separation. Zircon U-Pb-O isotopic analyses were carried out using the Cameca IMS 1280HR ion microprobe, following analytical procedures similar to Li et al. (2009, 2013a, 2013b). The ellipsoidal spot size is about 20 μm × 30 μm. Secondary standard zircons of Qinghu and Penglai were analyzed once every four or five spots as unknowns to monitor the reliability of U-Pb-O isotope analyses. Analyses of the standards yielded a concordant age of 159 ± 2 Ma ($n = 8$) for the Qinghu zircon and $\delta^{18}O$ values of 5.23 ± 0.20‰ ($n = 11$) for the Penglai zircon, within errors of their recommended values of 159.5 ± 0.2 Ma and 5.31 ± 0.10‰, respectively (Li et al., 2013a, 2013b). The uncertainties of a single analysis for U—Pb ages and O isotopes are reported at the 1σ and 2SE level, respectively. Data reduction of U—Pb age analyses was carried out using Isoplot/Ex 3 software (Ludwig, 2003).

Zircon Hf isotope analyses were performed on a Neptune Plus MC-ICP-MS (Thermo Scientific), coupled with a RESOlution M-50193 nm laser ablation system (Resonetics). The laser parameters were set as following: beam diameter, 45 μm; repetition rate, 6 Hz; energy density, ~4 J cm^{-2}. Helium was chosen as the carrier gas (800 ml min^{-1}). The mass bias of $^{176}Hf/^{177}Hf$ was normalized to $^{179}Hf/^{177}Hf = 0.7325$ with an exponential law. The detailed analytical procedure is reported in Zhang et al. (2015b). During the analytical sessions of this study, 46 analyses of the Plešovice zircon were collected yielding a weighted mean of $^{176}Hf/^{177}Hf = 0.282487 \pm 9$ (2SD), which is within error of the reported value (0.282482 ± 13 (2SD)) (Sláma et al., 2008).

Two samples of each rock type were chosen for in situ major and trace element analyses after detailed petrographic observation, which were performed on a Cameca SXFive FE Electron Probe Microanalyzer (EPMA). The operating conditions are: 15 kV accelerating voltage, 20 nA beam current, 5 μm beam diameter with peak counting times varying from 8 s to 40 s depending on the intensity of characteristic X-ray line and desired precision. Matrix corrections were based on the PAP (Pouchou and Pichoir) procedure (Pouchou and Pichoir, 1991). In situ trace element analyses of minerals were conducted using an ELEMENT XR (Thermo Fisher Scientific) ICP-SF-MS coupled with a 193-nm (ArF) Resonetics RESOlution M-50 laser ablation system. The detailed procedures are described in Zhang et al. (2019). Laser conditions were set as follows: beam size of 33 μm, repetition rate of 5 Hz, and energy density of ~4 J cm^{-2}. The calibration line for each element was constructed by analyzing the USGS reference glasses BCR-2G, BHVO-2G and GSD-1G with Si as an internal standard. The USGS reference glass TB-1G was measured as an unknown. Repeated analyses of TB-1G indicate that both precision and accuracy are better than 5% for most elements (e.g., Cr, Ni, Sr, Ba, Nb, Y and LREE). The major elements of the LA-ICPMS spots are represented by the average value of four EPMA analyses surrounding the LA-ICPMS spot.

Fresh samples from the Xinsi diorite ($n = 21$) and Tiechang gabbro ($n = 18$) were selected for whole-rock geochemical analyses, which were performed on a Rigaku RIX 2000 X-ray fluorescence spectrometer (XRF). The analytical uncertainties are between 1% (e.g., Si, Al, Mg, Fe, Ti and Ca) and 5% (e.g., Na and K). Trace element concentrations were determined using a Thermo iCAP Qc ICP-MS after acid digestion of samples in Teflon pressure vessels. The USGS and Chinese National standards AGV-2, GSR-1, GSR-2, GSR-3, BHVO-2, W-2a and SARM-4 were chosen for calibrating element concentrations of the analyzed samples. Analytical precision of the REE and other incompatible element analyses is typically 1%–5%.

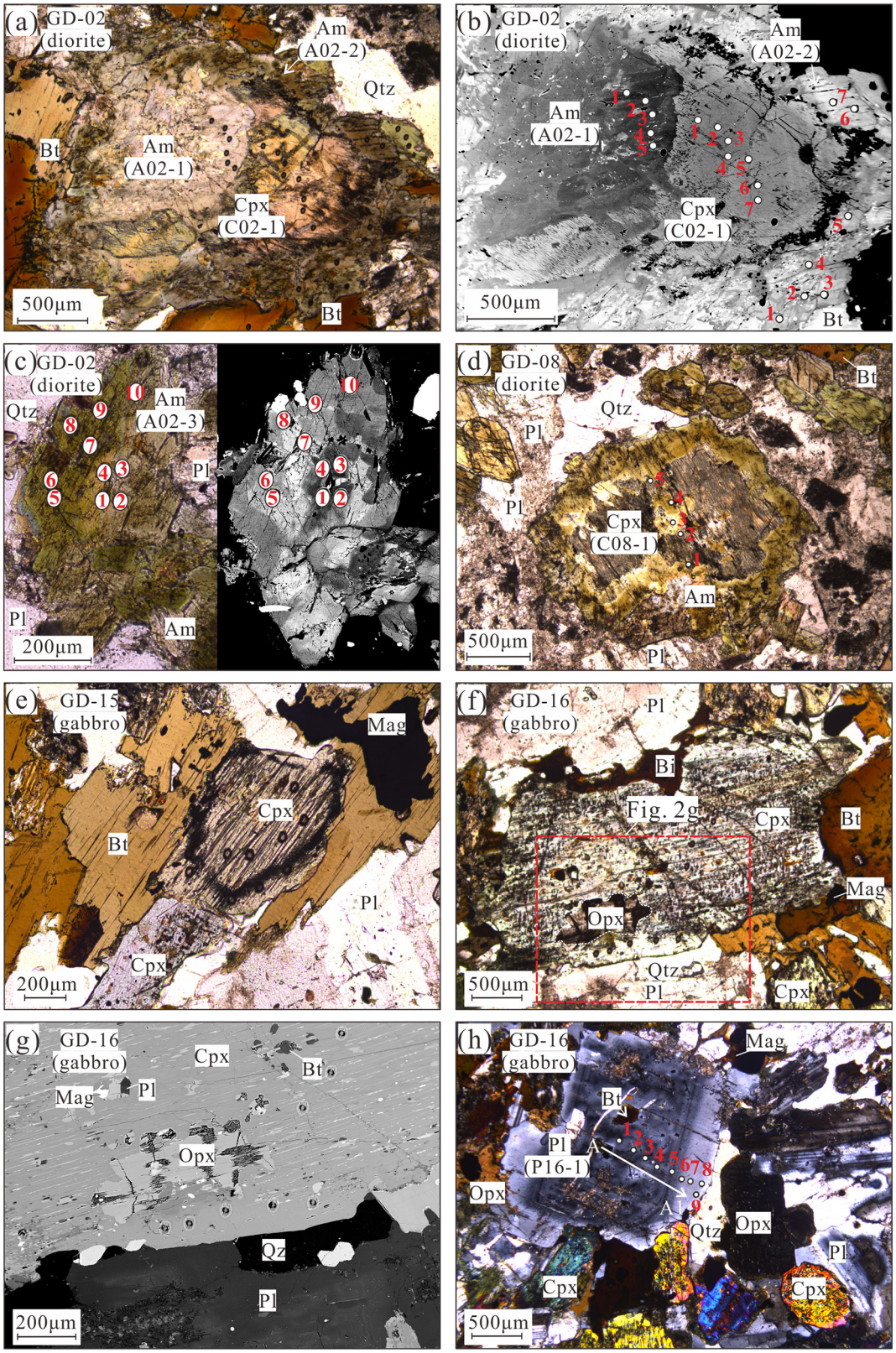

Fig. 2. Photomicrographs and BSE images illustrating the petrographic characteristics of the Xinsi diorite and Tiechang gabbro: (a, b) high-Mg clinopyroxene rim (C02–1) occurs around a high-Mg amphibole core (A02–1), with both replaced by later green amphibole rims (A02–2); (c) zoned amphibole (A02–3) consists of brown core and green rim; (d) low-Mg clinopyroxene (C08–1) was replaced by green amphibole in rim; (e, f, g) clinopyroxenes in the Tiechang gabbro contain abundant inclusions of orthopyroxene, biotite, plagioclase and magnetite; and (h) plagioclase (P16–1) in the Tiechang gabbro shows zonation texture. Circles and associated numbers denote the locations of LA-ICPMS analyzed spots for trace elements, and white line and letters indicate major element analytical transects. Abbreviations are as follows: amphibole (Am), biotite (Bt), clinopyroxene (Cpx), orthopyroxene (Opx), magnetite (Mag), plagioclase (Pl) and quartz (Qtz).

Representative samples from the Xinsi diorite ($n = 5$) and Tiechang gabbro ($n = 4$) were selected for whole-rock Sr and Nd isotopic analyses, which were conducted on a subset of whole-rock sample powders using a Neptune plus MC-ICP-MS. Detailed procedures of sample preparation and chemical separation are same as those described by Wei et al. (2002). The REE were separated using the cation exchange columns, and the Nd fractions were further separated by HDEHP-coated Kef columns. The procedure blanks were in the range of 200–500 pg for Sr and ≤ 50 pg for Nd. Measured $^{87}Sr/^{86}Sr$ and $^{143}Nd/^{144}Nd$ ratios were normalized to $^{86}Sr/^{88}Sr = 0.1194$ and $^{146}Nd/^{144}Nd = 0.7219$, respectively. Reference standards BHVO-2 were analyzed along with the unknowns, yielding $^{87}Sr/^{86}Sr$ ratio of 0.703489 ± 10 (2σ) and $^{143}Nd/^{144}Nd$ ratio of 0.512979 ± 6 (2σ), which are comparable to the recommended $^{87}Sr/^{86}Sr$ (0.703478 ± 34) and $^{143}Nd/^{144}Nd$ (0.512979 ± 14) ratios (Jochum et al., 2016).

4. Analytical results

4.1. Zircon U—Pb age and Hf—O isotope results

The zircons in the Xinsi diorite (Sample GD-1) and Tiechang gabbro (Sample GD-17) are all euhedral prismatic grains with large grain sizes (>150 μm; Fig. 3) and show oscillatory zoning in the CL images. The zircon U-Pb-Hf-O isotopic compositions for these samples are presented in Supplementary Tables 1 and 2, and shown in Fig. 3.

4.1.1. Xinsi diorite (GD-1)

Eighteen zircons were analyzed, which show variable Th (198–863 ppm) and U (111–683 ppm) contents with Th/U ratios of 0.45–0.85 (Supplementary Table 1). They have concordant U—Pb ages and yield a weighted mean $^{206}Pb/^{238}U$ age of 443 ± 3 Ma (MSWD = 0.31; Fig. 3a), which is interpreted as the crystallization age. These zircons have negative $\varepsilon_{Hf}(t)$ values (−9.2 to −5.2) and high $\delta^{18}O$ values (7.56 ± 0.14‰ to 8.22 ± 0.16‰) (Fig. 3c; Supplementary Table 2).

4.1.2. Tiechang gabbro (GD-17)

Seventeen zircons were analyzed, with variable Th and U concentrations (115–477 ppm and 82.9–645 ppm, respectively) and Th/U ratios of 0.71–1.35 (Supplementary Table 1). All U—Pb dating results are concordant and yield a weighted mean $^{206}Pb/^{238}U$ age of 440 ± 3 Ma (MSWD = 0.58; Fig. 3b), which is interpreted as the crystallization age. These zircons show negative $\varepsilon_{Hf}(t)$ values (−6.8 to −2.9) and high $\delta^{18}O$ values (8.17 ± 0.26‰ to 8.84 ± 0.15‰) (Fig. 3c; Supplementary Table 2).

4.2. Whole-rock geochemical and Sr—Nd isotopic compositions

Whole-rock geochemical and Sr—Nd isotopic compositions of samples from the Xinsi diorite and Tiechang gabbro are given in Supplementary Tables 3 and 4 and presented in Figs. 4, 5 and 6.

4.2.1. Xinsi diorite

The Xinsi diorites have narrow range of SiO_2 (54.0–56.0 wt%), MgO (7.98–10.7 wt%), K_2O (2.29–2.79 wt%), TiO_2 (0.73–0.91 wt%), Al_2O_3 (10.2–13.5 wt%) and Na_2O (1.20–1.85 wt%) with Mg# values from 0.63 to 0.69 (Fig. 4; Supplementary Table 3). The studied samples have slightly variable Cr (375–697 ppm), Ni (110–189 ppm), Ba

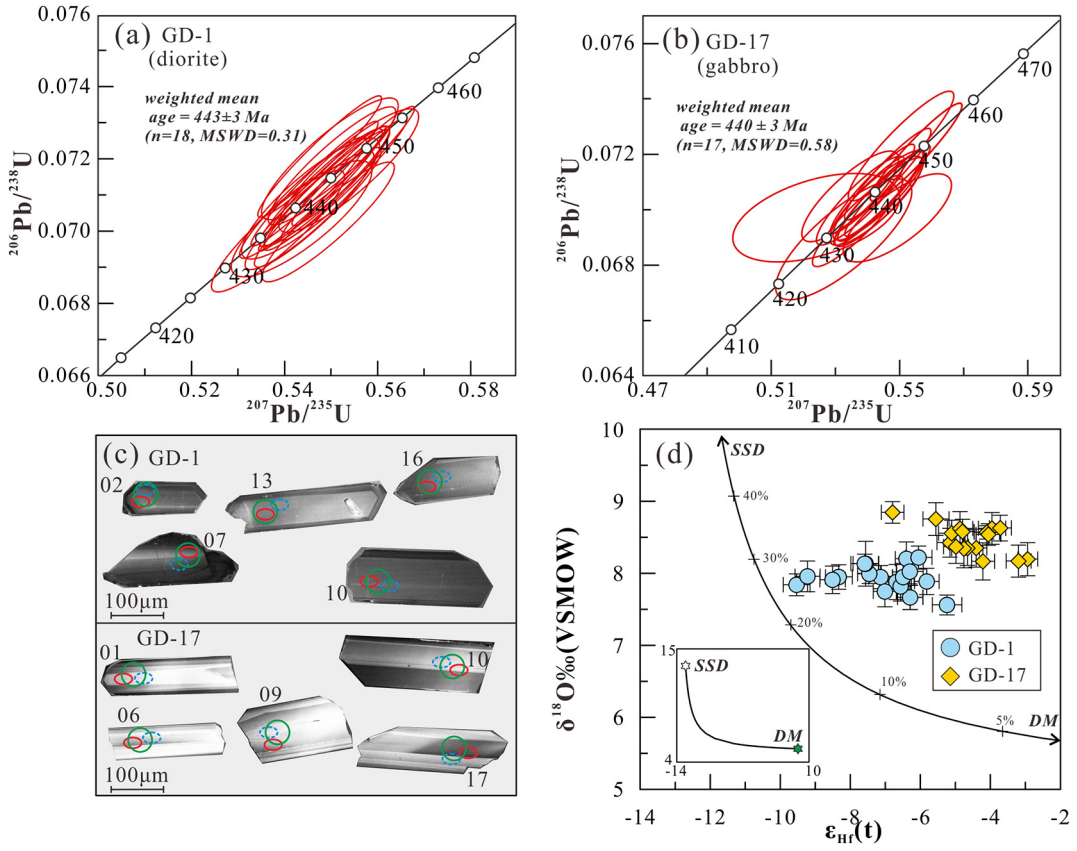

Fig. 3. (a, b) Concordia diagrams of SIMS U—Pb dating for zircons from the Xinsi diorite (GD-1) and Tiechang gabbro (GD-17); (c) Cathodoluminescence images showing locations of U—Pb age (red circle), Hf isotope (green circle) and O isotope (blue dashed circle) analyses (d) Zircon Hf—O isotope for the Xinsi diorite and Tiechang gabbro. The depleted mantle (DM)-subducted sediment (SSD) mixing line was calculated using $\varepsilon_{Hf}(t)$ values of +8 and − 12.5 and $\delta^{18}O$ values of 5.3‰ and 13.7‰, respectively. The Hf—O isotopic compositions of the SSD is represented by the Early Paleozoic granite (Huang et al., 2020).

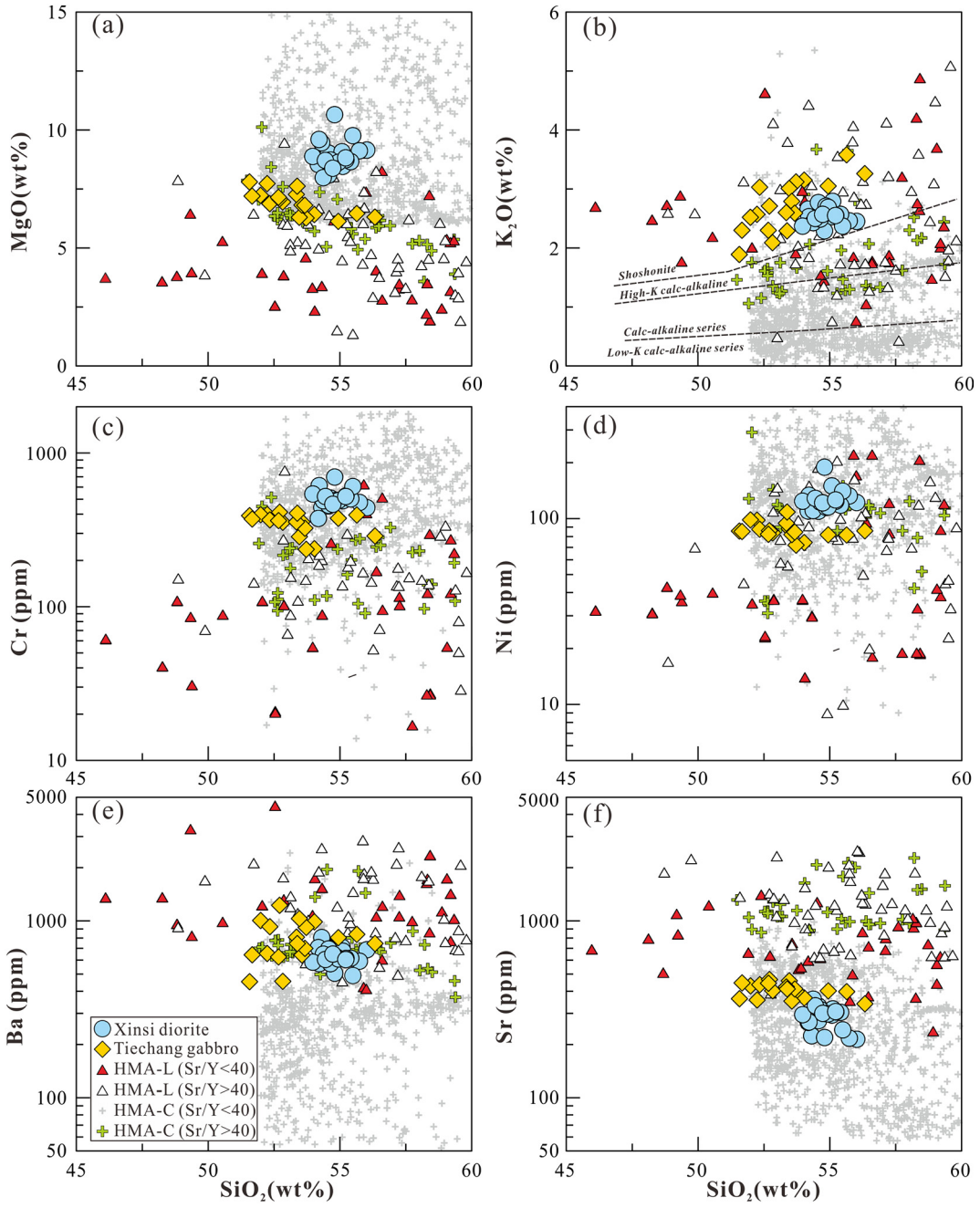

Fig. 4. Bivariate diagrams showing variations in the major and trace elements for the Xinsi diorite and Tiechang gabbro with the Cenozoic and Late Archean high-Mg andesitic rocks: (a) SiO_2 vs. MgO; (b) SiO_2 vs. K_2O; (c) SiO_2 vs. Cr; (d) SiO_2 vs. Ni; (e) SiO_2 vs. Ba; and (f) SiO_2 vs. Sr. Cenozoic high-Mg andesitic rocks (HMA-C) include high-Mg adakites (SiO_2 < 60 wt%; Mg# > 0.60; Sr/Y > 40) and high-Mg andesites (SiO_2 < 60 wt%; MgO > 6 wt%; Mg# > 0.60; Sr/Y < 40) from the modern subduction zones, which are compiled from the GEOROC database (http://georoc.mpch-mainz.gwdg.de/georoc/). Late Archean high-Mg andesitic rocks (HMA-L) are from Heilimo et al. (2010), Laurent et al. (2014), Lobach-Zhuchenko et al. (2008), Moyen et al. (2003), Shirey and Hanson (1984), Smithies and Champion (2000), Stern et al. (1989) and Stevenson et al. (1999).

(491–805 ppm) and Sr (214–361 ppm) (Fig. 4) and show low Sr/Y ratios (6.08–13.6) relative to typical adakite (Sr/Y > 40; Defant and Drummond, 1990). On a chondrite-normalized rare earth elements (REE) pattern (Fig. 5a), they are enriched in LREE ($[La/Yb]_N$ = 7.07–11.9) with negative Eu anomalies (Eu/Eu^* = 0.66–0.78). On a primitive mantle-normalized multi-element spider diagram, all of the samples are characterized by enrichment of large ion lithosphile elements (LILE), negative Nb-Ta-Ti anomalies and positive Pb anomalies (Fig. 5b). They show high initial $^{87}Sr/^{86}Sr$ ratios (0.7075–0.7086) and low initial $^{143}Nd/^{144}Nd$ ratios (0.511713–0.511731) with negative $\varepsilon_{Nd}(t)$ values (−6.9 to −6.6) (Fig. 6).

4.2.2. Tiechang gabbro

The Tiechang gabbros show wide range of SiO_2 (51.6–56.3 wt%) and K_2O (1.89–3.58 wt%) and have higher Al_2O_3 (12.7–15.1 wt%), TiO_2 (0.94–1.42 wt%), Na_2O (1.86–2.40 wt%), Sr (340–466 ppm), Ba (453–1225 ppm) and lower MgO (6.13–7.80 wt%), Cr (236–412 ppm) and Ni (72–109 ppm) and Mg# values (0.57–0.61) than the Xinsi diorites (Fig. 4), but with similar Sr/Y ratios (10.8–16.7). The Tiechang gabbros also show enrichment in LREE ($[La/Yb]_N$ = 7.96–11.7; Fig. 5c) with negative Eu anomalies (Eu/Eu^* = 0.64–0.92) on chondrite-normalized REE patterns, and exhibit LILE enrichment and pronounced negative Nb-Ta-Ti anomalies and positive Pb anomalies on primitive

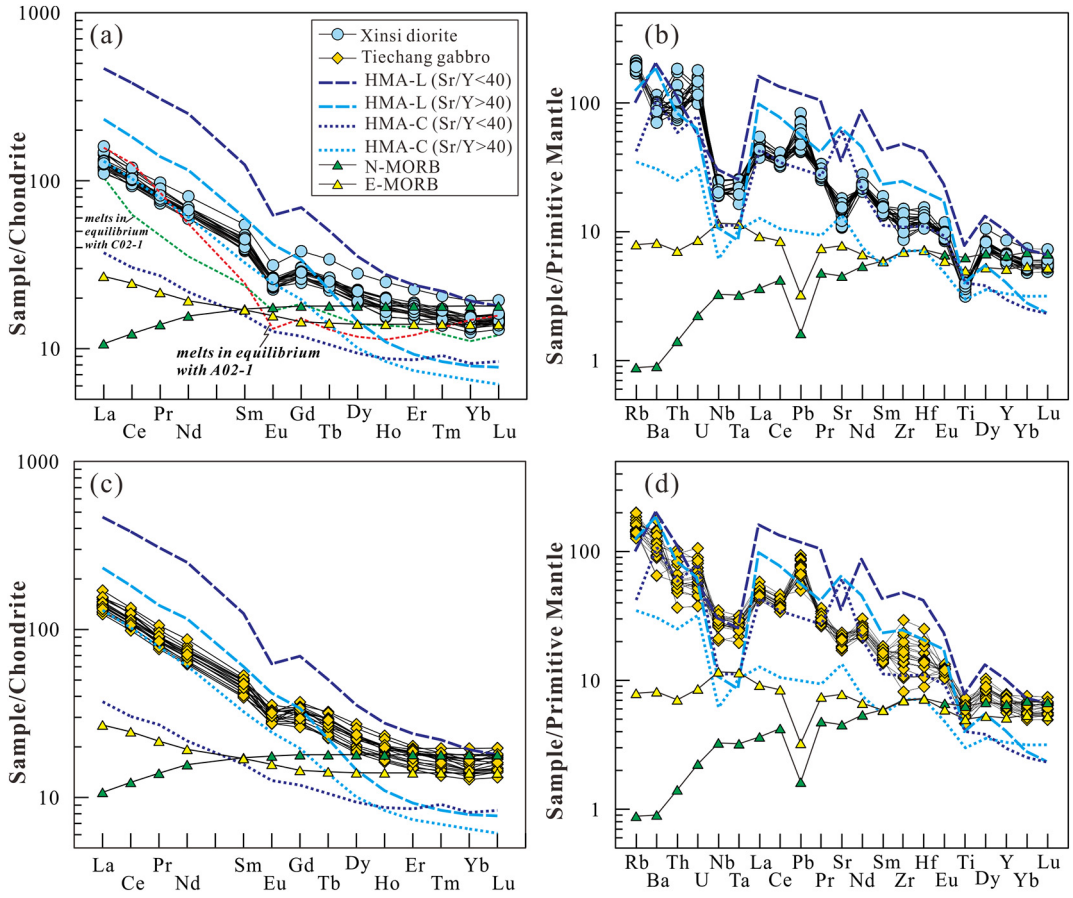

Fig. 5. Chondrite-normalized REE and primitive mantle (PM)-normalized trace element abundance for the Xinsi diorite and Tiechang gabbro. Data sources of the Cenozoic and Late Archean high-Mg andesitic rocks (HMA-C and HMA-L, respectively) are same as Fig. 4. Data of *E*-MORB and N-MORB and chondrite and PM normalization factors are from Sun and McDonough (1989). The REE patterns of the parental melts for the Xinsi diorites are calculated using representative composition of high-Mg clinopyroxne (C02–1) and amphibole (A02–1) with partition coefficients from Martin (1987) and McKenzie and O'Nions (1991), respectively.

mantle-normalized multi-element spider diagrams (Fig. 5d). They have high initial $^{87}Sr/^{86}Sr$ ratios (0.7064–0.7068) and low initial $^{143}Nd/^{144}Nd$ ratios (0.511837–0.511864) with negative $\varepsilon_{Nd}(t)$ values (−4.6 to −4.0) (Fig. 6).

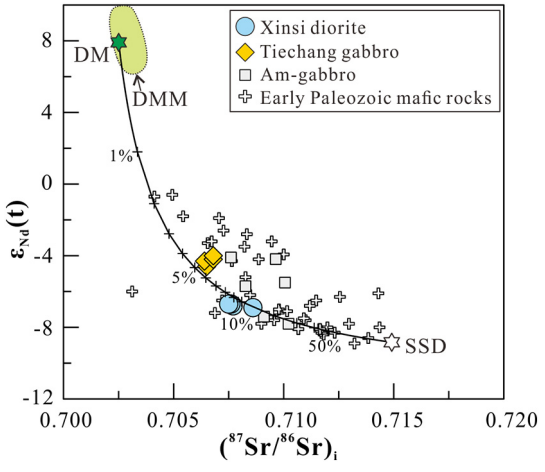

Fig. 6. $\varepsilon_{Nd}(t)$ vs. $(^{87}Sr/^{86}Sr)_i$ for the Xinsi diorite and Tiechang gabbro with previously reported amphibole-bearing gabbro (Am-gabbro) and other Early Paleozoic mafic rocks (Wang et al., 2013; Zhang et al., 2015a; Zhong et al., 2016). The data of depleted mantle (DM) and depleted MORB (DMM) are from Salters and Stracke (2004), and the subducted sediments (SSD) are represented by the Early Paleozoic upper crustal metasedimentary rocks from Wang et al. (2011).

4.3. Mineral compositions

The major and trace elemental compositions of amphibole, clinopyroxene, orthopyroxene, plagioclase and biotite in the Xinsi diorite and Tiechang gabbro samples are listed in Supplementary Tables 5–9.

4.3.1. Xinsi diorite

4.3.1.1. Clinopyroxene. Clinopyroxenes in the Xinsi diorite are mainly augite with subordinate diopside (Fig. S1), with compositions of $Wo_{38-48}En_{41-51}Fs_{8-14}$. They have variable Mg# values (0.76–0.87) and show wide range of Sr, Ba, Nb, Y and REE (Fig. 7; Supplementary Table 5). Compositions of representative crystals C02–1 and C08–1 are described as following:

Clinopyroxene C02–1 in sample GD-02 is an anhedral crystal partially surrounding a high-Mg amphibole core (A02–1), and both of them have a common rim consisting of green amphibole (A02–2) (Fig. 2a and b). C02–1 has high Mg# (0.80–0.87), Mg (0.90–0.98 apfu) and Cr (3516–5077 ppm) with low Sr (28.1–31.6 ppm), Ba (0.13–6.62 ppm), REE (25.6–42.2 ppm), Nb (≤0.23 ppm) and Y (11.7–16.2 ppm) (Figs. 7 and 8b). It is enriched in LREE and displays negative Eu anomaly ($Eu/Eu^* = 0.55–0.97$) on the chondrite-normalized REE patterns (Fig. 8a).

Clinopyroxene C08–1 in sample GD-08 is an anhedral crystal with a green amphibole rim (Fig. 2d). Compared with C02–1, C08–1 has lower Mg (0.81–0.85 apfu), Mg# values (0.75–0.83) and Cr (468–2741 ppm) and higher Ba (9.73–47.3 ppm), REE (66.7–185 ppm), Nb

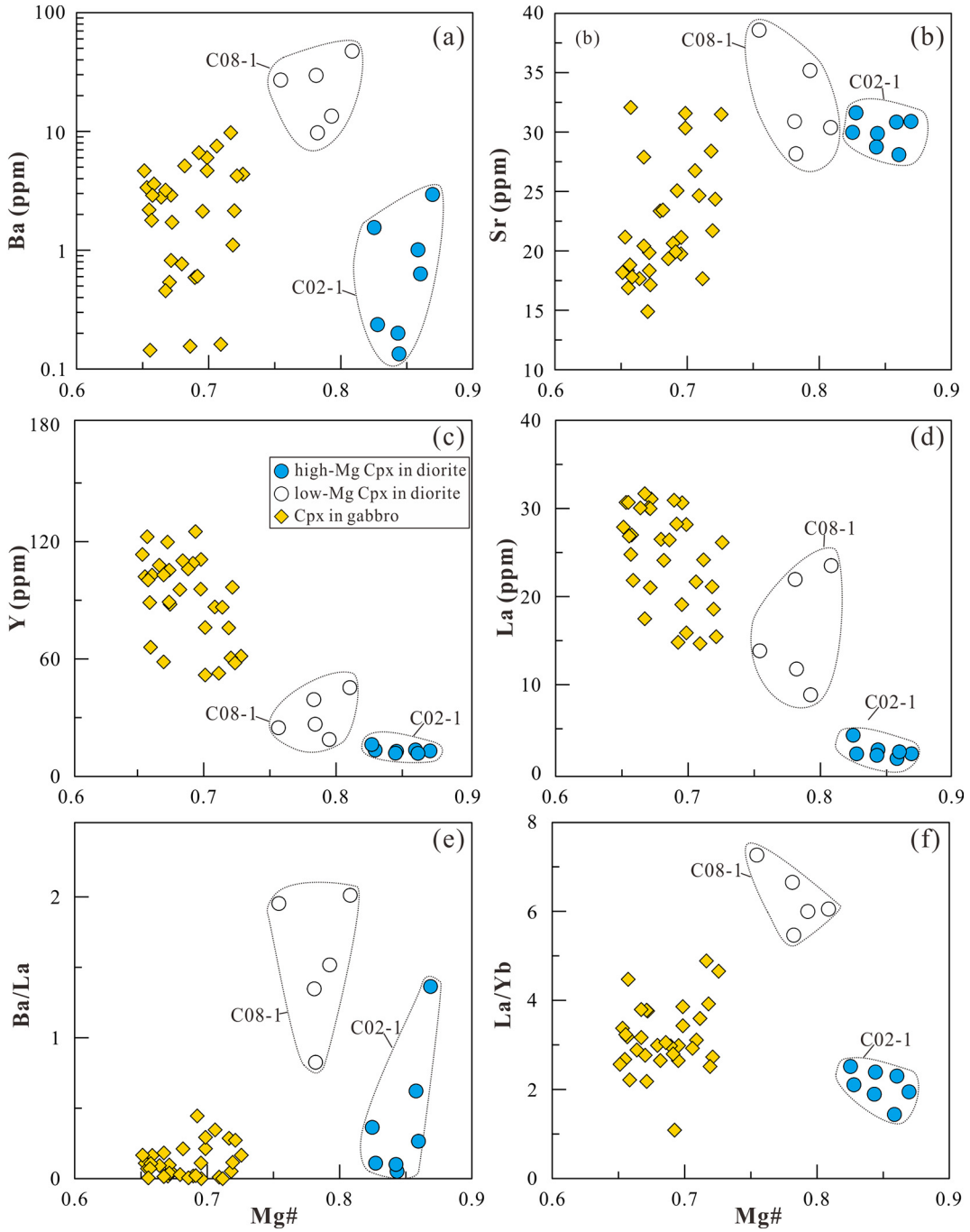

Fig. 7. Bivariate trace element plots of (a) Ba vs. Mg#; (b) Sr vs. Mg#; (c) Y vs. Mg#; (d) La vs. Mg#; (e) Ba/La vs. Mg#; (f) La/Yb vs. Mg# for clinopyroxenes in the Xinsi diorite and Tiechang gabbro.

(27.4–51.2 ppm) and Y (18.8–45.4 ppm) with similar Sr contents (28.2–38.6 ppm) (Figs. 7 and 8b). C08–1 is also LREE enriched ($[La/Yb]_N$ = 3.97–5.28) with negative Eu anomalies (Eu/Eu^* = 0.55–0.78) on the chondrite-normalized REE diagram (Fig. 8a).

4.3.1.2. Amphibole. Amphiboles in the Xinsi diorite are mainly classified as actinolite to magnesio-hornblende (Fig. S1) and have variable Si (6.64–7.92 apfu), Al (0.15–1.73 apfu), Mg (2.66–4.19 apfu) and Ti (0.01–0.20 apfu) with Mg# values of 0.60–0.83 (Fig. 9; Supplementary Table 6). They have variable Sr, Ba, Nb and REE contents, which are all negatively correlated with Mg# values (Fig. 9). Representative crystals A02–1, A02–2 and A02–3 in sample GD-02, with distinct compositions, are described as following.

Amphibole A02–1 occurs as a rounded crystal partially surrounded by clinopyroxene C02–1 and the amphibole rim of A02–2 (Fig. 2a) and has high Mg (3.76–4.19 apfu) and Mg# values (0.78–0.83) (Fig. 9). It has high Cr (1307–3126 ppm) and low Sr (10.4–15.7 ppm), Ba (0.43–16.3 ppm), Y (12.7–15.5 ppm), Nb (0.43–1.65 ppm) and REE (47.4–58.1 ppm) (Figs. 8c, d and 9), and is LREE-enriched ($[La/Yb]_N$ = 3.11–5.34) with negative Eu anomalies (Eu/Eu^* = 0.62–0.91) on the chondrite-normalized REE patterns (Fig. 8c).

Amphibole A02–2 occurs as rims surrounding the clinopyroxene C02–1 and amphibole A02–1 (Fig. 2a and b). Compared with A02–1, A02–2 has lower Mg (2.71–3.55 apfu), Mg# (0.61–0.73) and Cr (342–768 ppm), and higher Sr (23.6–88.2 ppm), Ba (31.5–142 ppm), Y (52.7–80.2 ppm), Nb (12.4–32.3 ppm) and REE (219–363 ppm)

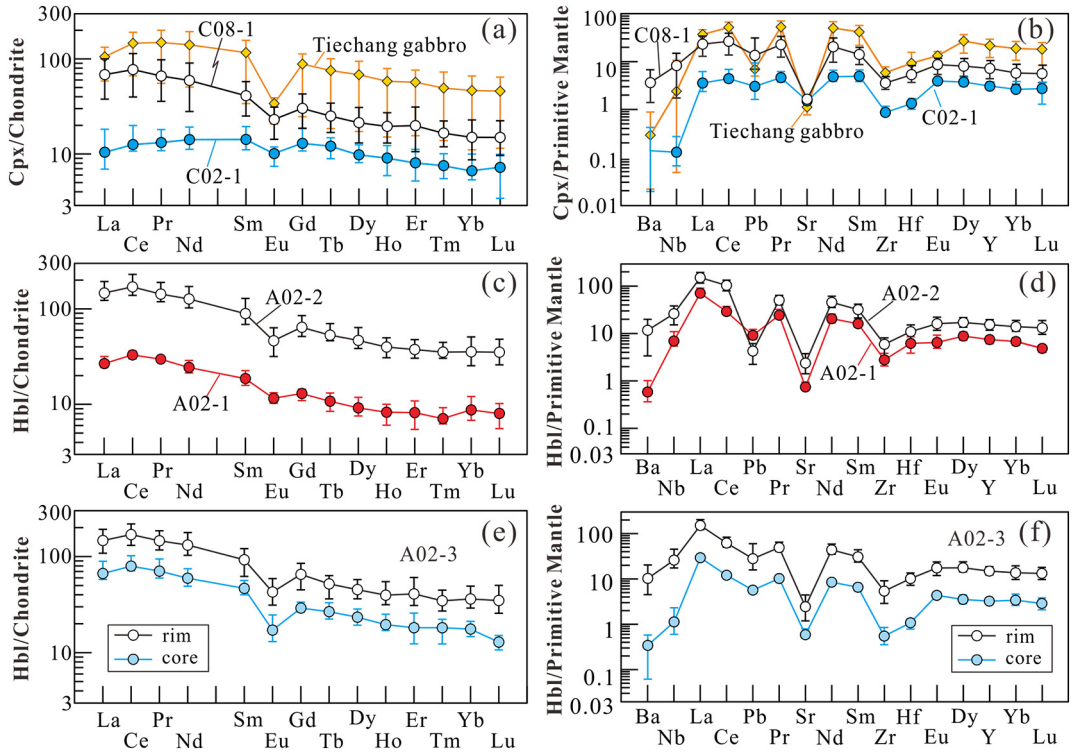

Fig. 8. Representative trace element abundance (average value) of (a, b) high-Mg (C02–1) and low-Mg (C08–1) clinopyroxene in the Xinsi diorite and clinopyroxene in the Tiechang gabbro; (c, d) high-Mg (A02–1) amphibole core and low-Mg green amphibole rim (A02–2) in the Xinsi diorite; (e, f) high-Mg brown core and low-Mg green rim of amphibole A02–3 in the Xinsi diorite, which are illustrated by the chondrite-normalized REE pattern and primitive mantle-normalized trace element patterns, respectively. Chondrite and PM normalization factors are from Sun and McDonough (1989).

(Fig. 8c and d). It is LREE-enriched ($[La/Yb]_N = 3.94–7.09$) with negative Eu anomalies ($Eu/Eu^* = 0.53–0.70$) on the chondrite-normalized REE patterns (Fig. 8c).

Amphibole A02–3 is a normally zoned crystal with brown core and green rim (Fig. 2c). The brown core has narrow range of Mg (3.28–3.41 apfu) and Mg# (0.68–0.71) (Fig. 9; Supplementary Table 6) with variable Sr (13.3–18.7 ppm), Ba (2.54–7.09 ppm), Y (26.1–37.6 ppm), Nb (3.87–7.80 ppm) and REE (109–162 ppm). It shows LREE-enriched rare earth elements patterns ($[La/Yb]_N = 4.54–5.82$) with negative Eu anomalies ($Eu/Eu^* = 0.36–0.55$; Fig. 8e). The green rim is in contact with plagioclase and quartz and has lower MgO (2.80–3.12 apfu) and Mg# values (0.63–0.67) than the brown core (Fig. 9; Supplementary Table 6). The rim is also higher in Ba (23.5–139 ppm), Sr (28.1–74.8 ppm), Nb (10.8–27.3 ppm), Y (50.3–84.4 ppm) and REE (209–358 ppm) than the core and shows similar chondrite-normalized REE patterns, with high $[La/Yb]_N$ values (4.47–6.62) and negative Eu anomalies ($Eu/Eu^* = 0.44–0.60$) (Fig. 8e and f).

4.3.1.3. Biotite. Biotites in the Xinsi diorite have variable Mg (2.48–3.12 apfu) and Mg# values (0.54–0.60) and are predominantly magnesio-biotites (Fig. S1). They have high Ba (2648–5065 ppm) and Nb (39.0–46.8 ppm), and low Sr (1.02–1.93 ppm) and Zr (0.45–1.82 ppm) (Fig. S2; Supplementary Table 7).

4.3.1.4. Plagioclase. Plagioclases in the Xinsi diorite show large range of An (anorthite) numbers (18–50; Fig. S3), with variable Sr (785–1064 ppm), Ba (63.7–93.0 ppm) and REE (24.4–60.6 ppm) (Fig. S2; Supplementary Table 8).

4.3.2. Tiechang gabbro

Clinopyroxenes in the Tiechang gabbro have lower Mg (0.69–0.88 apfu) and Mg# (0.56–0.74) than those in the Xinsi diorite, and mainly belong to augite and subordinate diopside (Fig. S1). Compared with the Xinsi clinopyroxenes, they also have lower Sr (14.9–32.1 ppm), Ba (0.14–5.99 ppm) and Nb (0.03–7.52 ppm), and higher Y (51.8–125 ppm) and REE (150–372 ppm), which poorly correlate with Mg# values (Fig. 7; Supplementary Table 5). These clinopyroxenes show LREE-enriched REE patterns with negative Eu anomalies ($Eu/Eu^* = 0.21–0.54$; Fig. 8a) on the chondrite-normalized REE patterns.

Orthopyroxenes in the Tiechang gabbro have narrow range of Mg (1.06–1.16 apfu) and Mg# values from 0.55 to 0.61 (Supplementary Table 9). Compared with clinopyroxene, they contain much lower Sr (0.80–5.51 ppm), Ba (0.40–6.00) and REE (16.2–27.9 ppm) and display LREE-depleted REE patterns ($[La/Yb)_N = 0.19–0.43$) with negative Eu anomalies ($Eu/Eu^* = 0.28–0.33$) (Supplementary Table 9).

Biotites in the Tiechang gabbro classify as magnesio-biotite with variable Mg (2.78–3.30 apfu) and Mg# values (0.53–0.61) (Fig. S1; Supplementary Table 7) and have lower Ba (1287–2014 ppm) than those in the Xinsi diorite (Fig. S2; Supplementary Table 7).

Plagioclases in the Tiechang gabbro are mainly andesine and labradorite with An numbers from 40 to 64 (Fig. S3; Supplementary Table 8) and have lower Sr (606–768 ppm) than those in the Xinsi diorite (Fig. S2). Some of the plagioclases (such as P16–1) show normal zoning texture with slightly higher An numbers (42–58) in the core than the rim (41–43) (Fig. S4). However, the Sr and Ba contents of the core (606–768 ppm and 143–202 ppm, respectively) are similar to those of the rim (Sr = 706–723 ppm; Ba = 108–161 ppm) (Fig. S4).

5. Discussion

5.1. Pressure and temperature during magmatic evolution

Amphiboles and clinopyroxenes in the Xinsi diorite have variable Mg# values (Figs. 7 and 9), suggesting their formation from melts that had undergone varying degrees of magmatic differentiation. The high Mg# values (up to 0.87) in clinopyroxene C02–1 suggest that the crystal was in equilibrium with a melt of Mg# values up to 0.71, based on the Fe—Mg exchange coefficient between clinopyroxene and mafic melts

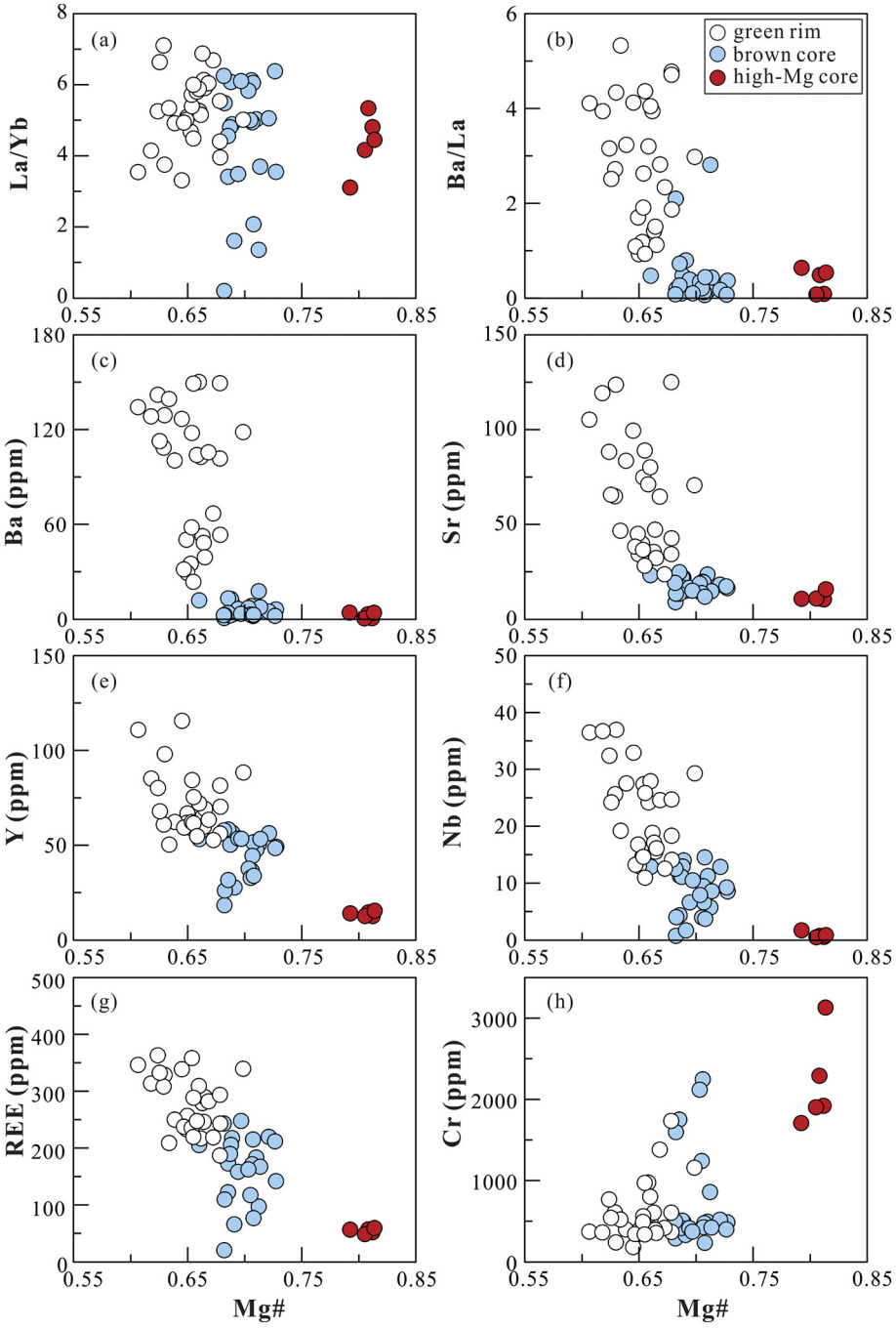

Fig. 9. Bivariate trace element plots of (a) La/Yb vs. Mg#; (b) Ba/La vs. Mg#; (c) Ba vs. Mg#; (d) Sr vs. Mg#; (e) Y vs. Mg#; (f) Nb vs. Mg#; (g) REE vs. Mg# and (h) Cr vs. Mg# for amphiboles in the Xinsi diorite.

of Kinzler (1997). This indicates that C02–1 should have crystallized during the initial stage of magmatic evolution. The C02–1 clinopyroxene occurs as a rim around high-Mg amphibole A02–1, indicating that the amphibole crystallized before or at the same time as clinopyroxene C02–1. Both C02–1 and A02–1 show negative Eu anomalies, indicating that plagioclases precipitated coeval with or prior to these minerals. These textural relationships demonstrate that the early magmatic evolution of the parental melts for the Xinsi diorite involved fractional crystallization of clinopyroxene, amphibole, and plagioclase. Experimental studies show that the co-precipitation of amphibole, clinopyroxene and plagioclase in mafic magmatic systems commonly occurs under relatively low pressures (~4 kbar) and high H_2O contents (Moore and Carmichael, 1998). This suggests that the parental melt of the Xinsi diorite might have evolved at upper crustal levels. The compositions of the amphibole rim and neighboring plagioclase, both of which are in contact with quartz (Fig. 2c), were used to estimate temperature and pressure conditions during formation of the Xinsi diorite, using the Al-in-hornblende geobarometer (Schmidt, 1992) and the amphibole-plagioclase geothermometer (Holland and Blundy, 1994). These calculations yielded pressures of 3.1–4.4 (±0.6) kbar and temperatures of 633–740 (±40) °C, which are consistent with the early crystallization of amphibole, clinopyroxene and plagioclase during the initial stage of magmatic evolution. Thus, the parental melts of the Xinsi diorite probably evolved in the upper crust.

The clinopyroxene and orthopyroxene in the Tiechang gabbro show negative Eu anomalies (Fig. 8; Supplementary Table 9), indicating that

they crystallized in the presence of plagioclase. This is consistent with the occurrence of plagioclase inclusions in the clinopyroxenes (Fig. 2g). Some plagioclases (e.g., P16–1) are zoned (Fig. 2h), which is related to their magmatic evolution. The rim compositions of coexisting clinopyroxene, orthopyroxene and plagioclase (Fig. 2h) can be used to evaluate the pressure and temperature conditions of their magma chamber using the two-pyroxene geothermometer of Wells (1977) and the pyroxene-plagioclase geobarometer of McCarthy and Patino Douce (1998), which indicate pressures of 5.7–6.3 kbar and temperatures of 925–997 °C. The parental melts of the Tiechang gabbro thus mostly likely evolved at middle to lower crustal depths.

5.2. Magmatic evolution for the Xinsi diorite and Tiechang gabbro

Mineral compositions are closely related to the parental melt composition (Hermann et al., 2001). Amphiboles, clinopyroxenes, biotites and plagioclases in the studied samples have highly variable incompatible element concentrations (i.e., REE, Nb, Y, Sr and Ba; Figs. 7 and 9), which potentially record details of their magmatic evolution process.

The Xinsi diorites show lower Mg# values (0.63 to 0.69) than primary melts generated by the partial melting of mantle peridotite (Mg# ≥ 0.72), indicating fractionation of Mg-rich minerals during early magma evolution of their parental melts. The chemical signature of their parental melts may be documented in the early-stage minerals in the Xinsi diorites, like the high-Mg clinopyroxenes (C02–1) and cores of amphiboles (A02–1, A02–3). These minerals all have low Ba, Sr, Nb, Y and REE contents (Figs. 7 and 9), indicating low concentrations of these incompatible elements in their parental melts during the early stage of magmatic evolution. For example, the melts in equilibrium with high-Mg amphibole A02–1 should have low Ba (~33.7 ppm), Sr (~131 ppm), Nb (~2.06 ppm), Yb (~3.5 ppm) and Y (~33.2 ppm) with low Sr/Y ratios (~3.95), as determined using partition coefficients for these elements in basaltic systems (McKenzie and O'Nions, 1991). The Xinsi diorites contain higher concentrations of Sr, Ba, Y, Nb and Yb abundances than their parental melts, indicating enrichments of these incompatible elements during the magmatic evolution process.

The low-Mg clinopyroxene (e.g., C08–1) in the Xinsi diorite has much higher concentrations of Ba, REE, Nb and Y than the high-Mg clinopyroxene (C02–1) (Fig. 8a and b), which would be due to the enrichment of these incompatible elements during magmatic evolution. On the other hand, the partition coefficients for these elements can vary significantly in different types of clinopyroxenes (Qian et al., 2015). The incompatible elements, such as REE, Zr and Y, tend to have higher partition coefficients in low-Mg clinopyroxene than in high-Mg clinopyroxene (Qian et al., 2015), which may partially account for the distinct compositions between C08–1 and C02–1. In addition, C08–1 and C02–1 have similar Sr contents despite their different Mg# values, which is reasonable because Sr has similar partition coefficients in high-Mg and low-Mg clinopyroxenes (Qian et al., 2015). In addition, it is noteworthy that the low-Mg clinopyroxene C08–1 has lower Eu/Eu^* values than the high-Mg clinopyroxene C02–1 (Fig. 8a), which is likely due to plagioclase fractionation. Since plagioclase shows much higher partition coefficients for Sr than Ba, REE, Nb and Y (Dunn and Sen, 1994), fractional crystallization of plagioclase can cause elemental fractionation between Sr and other incompatible elements (e.g., Ba, REE and Nb) in residual melts. Thus, the distinct compositions for low-Mg (C08–1) and high-Mg clinopyroxenes (C02–1; Fig. 8a and b) can reflect compositional change of melts with significant enrichment of incompatible elements (e.g. Ba, Nb, REE and Y) through fractionation of plagioclase and mafic minerals (e.g., amphibole and clinopyroxene) during the early stage of magmatic evolution process. On the other hand, the rim of normally zoned amphibole A02–3 (Fig. 2c) has lower Mg# values (0.60–0.67) and much higher REE, Nb, Y, Sr and Ba contents than the core (Mg# = 0.68–0.70; Fig. 8e and f), denoting negative correlations between incompatible elements (Sr, Ba, Nb, Y and REE) and Mg# values (Fig. 9). This points to magmatic differentiation that was controlled by the fractionation of dominant Mg-rich minerals (e.g., clinopyroxene) during the later stage evolution process, while the crystallization of plagioclase and biotite, which contain extremely high Sr and Ba (Fig. S2), was insignificant.

The Tiechang gabbros show lower Mg# values (0.57–0.61) than the Xinsi diorites (Mg# = 0.63–0.69), indicating that their parental melts experienced significant crystallization of Mg-rich minerals, which may also be the reason for high Sr and Ba in the Tiechang gabbro samples. However, the clinopyroxenes in the Tiechang gabbro show poor correlations between Mg# and Ba, and Mg# and Sr, and normally zoned plagioclase P16–1 has similar concentrations of Ba and Sr between the core and the rim (Fig. S4), which might not record the process of enriching incompatible trace elements in the parental melts during magmatic evolution. The low Mg# (0.56–0.74) values of clinopyroxene (Fig. 7) and the low An (41–58) of plagioclase P16–1 (Fig. S4) in the Tiechang gabbro suggest that these minerals possibly formed during the late stage of magmatic evolution. It is therefore difficult to determine the enrichment process of incompatible elements for the Tiechang gabbro, given the absence of early stage mineral phases.

The Tiechang gabbros and Xinsi diorites all show high MgO, SiO_2 and K_2O, resembling those of high-Mg andesitic rocks (Fig. 4). This suggests similar partition coefficients between minerals and melts during the magmatic evolution of the two rocks types. The Tiechang gabbro samples have higher whole-rock Sr and Ba contents than the Xinsi diorite samples (Fig. 4). If high Ba and Sr in the Tiechang gabbro were inherited from their sources, then their parental melts should be much higher in these elements than the Xinsi diorites. However, the clinopyroxenes, plagioclases and biotites in the Tiechang gabbro samples all have lower Sr and Ba contents than the equivalent phases in the Xinsi diorite samples (Figs. 7 and S2), indicating their crystallization from low-Sr and low-Ba melts. Therefore, the relatively low Mg# values and high Ba and Sr in the Tiechang gabbro indicate that their parental melts experienced significant crystallization of Mg-rich minerals (~60%), which led to the enrichment in Ba and Sr. In addition, the Tiechang gabbros show negative Eu anomalies (Fig. 5c), also excluding the possibility of feldspar accumulation as a mean for enriching Ba and Sr in the studied samples.

5.3. Mantle sources of the Xinsi diorite and Tiechang gabbro

The Xinsi diorites and Tiechang gabbros show high SiO_2, K_2O and Ba contents, high $^{87}Sr/^{86}Sr$ ratios, negative $\varepsilon_{Nd}(t)$ values, negative zircon $\varepsilon_{Hf}(t)$ values and heavy zircon O isotopic compositions (Figs. 3 and 6), which could have been inherited from their parental melts or induced by crustal assimilation. However, crustal assimilation, if it occurred, would be an insignificant influence on the chemical compositions of the studied samples. Firstly, these samples exhibit high MgO, Cr and Ni that are not correlated with SiO_2 (Fig. 4), excluding significant inputs of crustal materials to the parental melts. Secondly, these samples have Ba and Sr contents even higher than the upper crustal sedimentary rocks represented by paragneiss enclaves in the Early Paleozoic granite (Sr = 65.4–254 ppm; Ba = 446–1013 ppm; Wang et al., 2011).

Hence, the Xinsi diorites and Tiechang gabbros are all enriched in both mantle (Mg, Cr and Ni) and crustal (Si, Sr and Ba) elements, resembling typical high-Mg andesitic characteristics (Fig. 4). High-Mg andesitic melts may be generated by the interaction of high-Sr magmas (from delaminated crust or a subducted slab) with mantle peridotite (Rapp et al., 1999; Shirey and Hanson, 1984; Stern et al., 1989) or can be produced directly by the partial melting of an enriched mantle source that was metasomatized by melts derived from subducted slab (Tatsumi, 2006). High-Mg andesitic rocks that evolve from high-Sr magmas assimilated by mantle peridotite commonly have low HREE contents, because these elements are partitioned into residual garnet in the source during the melting of delaminated crust or subducted slab (e.g., Kay, 1978). However, the Xinsi diorite and Tiechang gabbro samples all have high HREE contents (Fig. 5), which excludes the possibility of abundant garnet residual in their source(s). In addition, the genetic

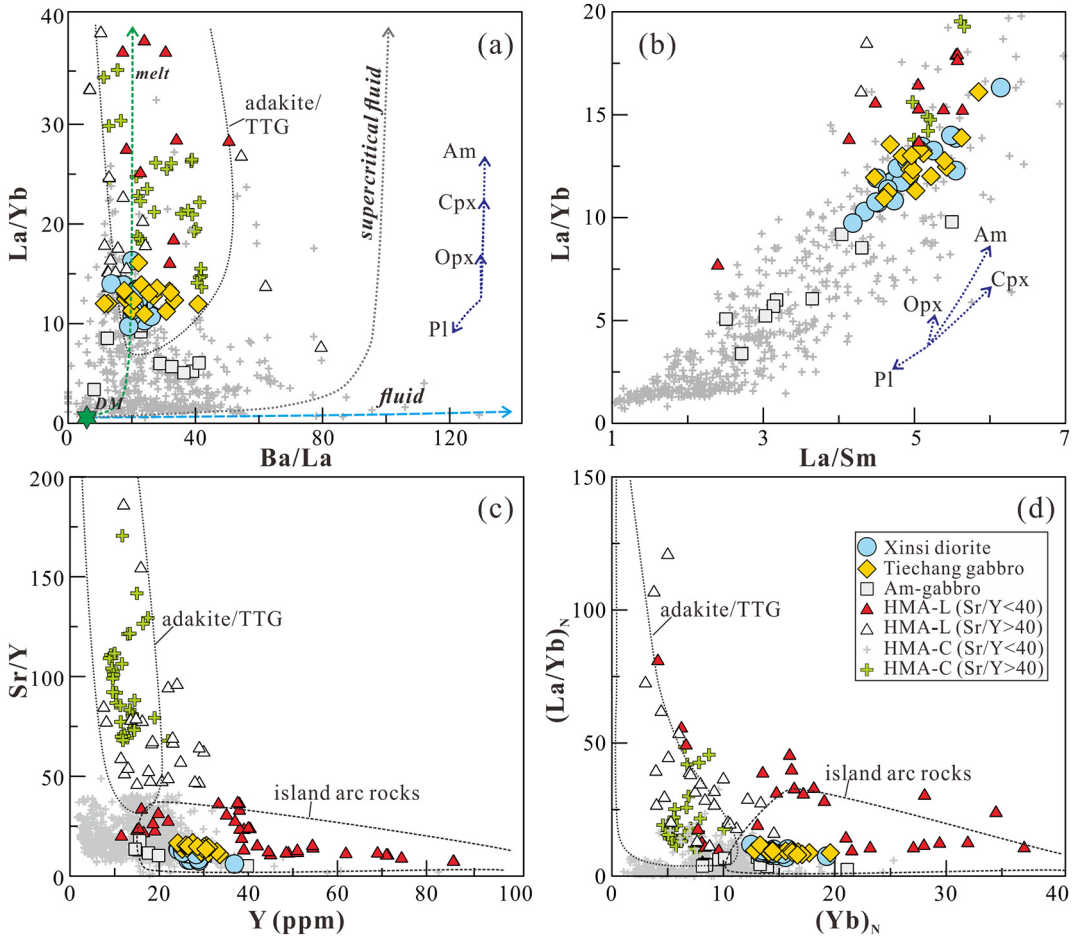

Fig. 10. Bivariate trace element plots of (a) Ba/La vs. La/Yb; (b) La/Yb vs. La/Sm; (c) Sr/Y vs. Y; (d) $(La/Yb)_N$ vs. $(Yb)_N$ for the Xinsi diorite and Tiechang gabbro. The fractional crystallization trends of amphibole (Am), clinopyroxene (Cpx), orthopyroxene (Opx) and plagioclase (Pl) are shown by dashed arrows. Fluid, supercritical fluid and melt from the subducted sediments (GLOSS; Plank and Langmuir, 1998) are represented by blue, grey and green dashed arrows, respectively. Fluid, supercritical fluid and melt from the subducted sediments (GLOSS; Plank and Langmuir, 1998) are represented by blue, grey and green dashed arrows, respectively. Compositions of fluids and melts are calculated with conditions similar to those in Yu et al. (2020), and compositions of supercritical fluid are calculated using partition coefficients from Kessel et al. (2005) (900 °C, 4 GPa). Data source of the Cenozoic and Late Archean high-Mg andesitic rocks (HMA-C and HMA-L, respectively) are same as Fig. 4.

model for high-Mg andesite evolved from high Ba and high Sr parental melts (Shirey and Hanson, 1984; Smithies and Champion, 2000; Stern et al., 1989) is also inconsistent with the low Ba and Sr concentrations of the inferred parental melts for the Xinsi diorite and Tiechang gabbro. Thus, we suggest that the Xinsi diorites and Tiechang gabbros were derived from the partial melting of mantle sources rather than results of the interaction between crust-derived high-Si magmas and mantle peridotite.

The Xinsi diorites and Tiechang gabbros both have high $^{87}Sr/^{86}Sr$, negative whole-rock $\varepsilon_{Nd}(t)$, negative zircon $\varepsilon_{Hf}(t)$ and high zircon $\delta^{18}O$ values (Figs. 3c and 6), suggesting an origin from enriched lithospheric mantle instead of the depleted asthenospheric mantle. This is also consistent with the relatively fractionated REE patterns of the parental melts in equilibrium with early-stage minerals such as amphibole A02–1 and clinopyroxene C02–1 (Fig. 5a). Liu et al. (2018) suggested that some of the Early Paleozoic high-Mg andesitic rocks in the Yunkai domain were generated by the partial melting of the mantle wedge metasomatized by slab-derived fluids and/or melts due to the subduction of the Huanan oceanic crust beneath the Cathaysia Block. In contrast, the Early Paleozoic amphibole gabbros in the Xinsi and Tiechang areas (Fig. 2) were suggested to derive from the partial melting of an enriched mantle source that had undergone metasomatism by melts from subducted slab during the Late Neoproterozoic (~1 Ga; Wang et al., 2013). During this subduction, the down-going slab would have undergone dehydration and partial melting and release fluids and melts that interact with the overlying depleted mantle wedge. The slab-derived materials would compositionally overprint the mantle, yielding the enriched Sr—Nd isotopic compositions of arc rocks (e.g., Chauvel et al., 2009). Modeling shows that ~5–10% input of subducted sediments to the mantle would be necessary to account for the observed Sr—Nd isotopic composition of the Xinsi diorite and Tiechang gabbro (Fig. 6), which is higher than in modern subduction zones (mostly <5%; Chauvel et al., 2009). Therefore, it is reasonable to suggest that the enriched Sr—Nd isotopes of the studied samples may not be completely attributed to subduction but may be partly caused by the long-term residence of crustal materials in the mantle source (Wang et al., 2013). The Xinsi diorites and Tiechang gabbros are located far away (~500 km) from the supposed Early Paleozoic subduction zone near the Yunkai domain (Fig. 1a). These rocks therefore cannot be the products of the Early Paleozoic subduction of the Huanan Ocean beneath the Cathaysia Block. On the other hand, Early Paleozoic subduction events might not have occurred in the South China Block because: (1) there is a lack of ophiolite and syntectonic high-pressure metamorphic rocks; and (2) it was predominantly a neritic-bathyal sedimentary setting (Li et al., 2010; Wang et al., 2011). In addition, mafic and felsic rocks of the Wuyi-Yunkai Orogen all have negative whole-rock $\varepsilon_{Nd}(t)$ and zircon $\varepsilon_{Hf}(t)$ values, indicating an insignificant input of juvenile materials in the petrogenesis (Fig. 6; Wang et al., 2013; Yu

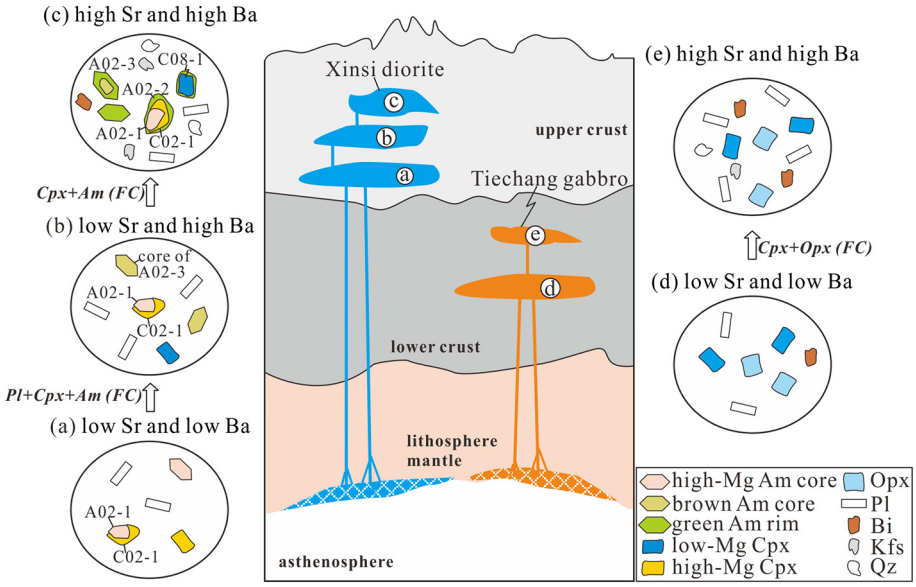

Fig. 11. Schematic diagrams showing magmatic evolution processes, including crystallization sequence and enrichment of Sr and Ba, in the Xinsi diorite (a-c) and Tiechang gabbro (d-e). (a) The parental melts of the Xinsi diorite have low Ba and Sr, (b) enriching Ba by fractional crystallization (FC) of Pl and Mg-rich minerals (e.g., Cpx and Am), and (c) enriching Sr and Ba by fractional crystallization of Mg-rich minerals (e.g., Cpx and Am); (d) the parental melts of the Tiechang gabbro are initially low in Ba and Sr, and (e) enriching Ba and Sr by the fractionation of Mg-rich minerals (e.g., Cpx and Opx).

et al., 2016). Therefore, we propose that the Xinsi diorites and Tiechang gabbros formed in an intracontinental orogenic setting and were generated by the partial melting of an enriched mantle source that had been refertilized during ancient subduction events.

Subducted slab-derived components can be recycled into the mantle wedge via fluids, supercritical fluids and melts, which have different capacities in mobilizing element from subducted slab (Hermann et al., 2006; Spandler et al., 2007; Woodhead et al., 2001). For example, Ba may be transferred from subducted slab to the mantle wedge by relatively low-temperature fluids, whereas LREE, high-field-strength elements (HFSEs, e.g., Nb) and HREE (e.g., Yb) may be retained in monazite (or allanite), rutile and garnet in subducted slab (Woodhead et al., 2001). This will result in high Ba/La and low La/Yb ratios in the released fluids (Fig. 10; Woodhead et al., 2001). High temperature supercritical fluids (700–900 °C; 4–6 GPa) can mobilize Ba (D_{Ba} = 6.1–65) and La (D_{La} = 0.28–17.6) more effectively than Nb (D_{Nb} = 0.056–3.7) and Yb (D_{Yb} = 0.004–0.02; $D = C_{liquid}/C_{solid}$ where C denotes element concentrations; Kessel et al., 2005), and may have high Ba with high Ba/La and La/Yb ratios (Fig. 10). In contrast, the melting of subducted slab can mobilize LREE into the resulting melts due to the breakdown of monazite and/or allanite, while Ba, Nb and Yb can be retained in phengite, rutile and garnet, respectively (Hermann and Rubatto, 2009). Thus, melts from subducted slab are characterized by high La/Yb and low Ba/La ratios (Woodhead et al., 2001). As the Xinsi diorite and Tiechang gabbro samples are all characterized by high La/Yb and low Ba/La ratios (Fig. 10a), their mantle sources might have been metasomatized by melts from subducted slab and associated sediments. However, the amphiboles and clinopyroxenes in the Xinsi diorite and Tiechang gabbro samples show variable Ba/La and La/Yb ratios with different Mg# values (Figs. 7 and 9), indicating that the melt compositions had changed during magmatic differentiation. One key issue is whether the parental melts of the Xinsi diorite and Tiechang gabbro are characterized by high La/Yb and low Ba/La ratios.

Amphiboles from the Xinsi diorite samples show variable Mg# values (0.60–0.81) that negatively correlate with Ba/La ratios but are uncorrelated with La/Yb (Fig. 9). This suggests elevation of Ba/La ratio in the residual melts during magmatic differentiation, while the La/Yb ratios may have not significantly changed. The insignificant change of La/Yb ratios in the residual melts is also evidenced by the similar REE patterns between the Xinsi diorites and the modeling parental melts in equilibrium with high-Mg clinopyroxene C02–1 and amphibole A02–1 (Fig. 5a), which crystallized during the initial stage of magmatic evolution. On the other hand, clinopyroxene and amphibole have similar partition coefficients for La (Kd_{La}^{Cpx} = 0.0536; Kd_{La}^{Am} = 0.17) and Ba (Kd_{Ba}^{Cpx} = 0.00068; Kd_{Ba}^{Am} = 0.12; Hart and Dunn, 1993; McKenzie and O'Nions, 1991), while partition coefficient of La (Kd_{La}^{pl} = 0.075) in plagioclase is much lower than Ba (Kd_{Ba}^{pl} = 0.38; Dunn and Sen, 1994). Thus, elevation of Ba/La in melts should not be caused by fractional crystallization of clinopyroxene, amphibole and plagioclase (Fig. 10). In the Xinsi diorite, Ba is mainly hosted in K-rich minerals, such as biotite (Fig. S2), which are anhedral and mainly occur as interstitial phases between other minerals in the Xinsi diorite. This suggests that these K-rich minerals should crystallized during late stage of magmatic evolution process, which is responsible for enrichment of Ba in melts, as revealed by negative correlation between Ba and Mg# in amphibole in the Xinsi diorite (Fig. 9). In addition, La is incompatible in the major phases (e.g. Cpx, Am and Pl) but is enriched in accessory minerals, such as apatite and monazite (Bea, 1996). Crystallization of these accessory minerals may cause fractionation of Ba and La and could increase the Ba/La ratios of the residual melt. This indicates that the parental melts for the Xinsi diorites should have lower Ba/La and similarly high La/Yb ratios compared with these dioritic samples. The Tiechang gabbros show different REE patterns with negative Eu anomalies ($Eu/Eu^* = 0.64–0.92$; Fig. 5), and the variations in their La/Yb and La/Sm ratios are indicative of clinopyroxene and plagioclase fractionation (Fig. 10b). This suggests that the fractionation of clinopyroxene could be responsible for the high La/Yb ratios of the Tiechang gabbro. However, the clinopyroxenes in the Tiechang gabbro have La/Yb and Ba/La that correlate poorly with Mg# values (Fig. 7), indicating insignificant changes in the La/Yb and Ba/La ratios of their parental melts. Therefore, the parental melts for the Tiechang gabbro are also characterized by high La/Yb and low Ba/La ratios.

Collectively, the parental melts for the Xinsi diorite and Tiechang gabbro appear to have high La/Yb and low Ba/La ratios, illustrating that their mantle sources were metasomatized by melts derived from subducted slab and associated sediments during ancient subduction events.

5.4. New petrogenetic model for high-Mg andesite

The Cenozoic high-Mg andesitic rocks mainly include the circum-Pacific high-Mg adakites and high-Mg andesites (e.g., Kay, 1978;

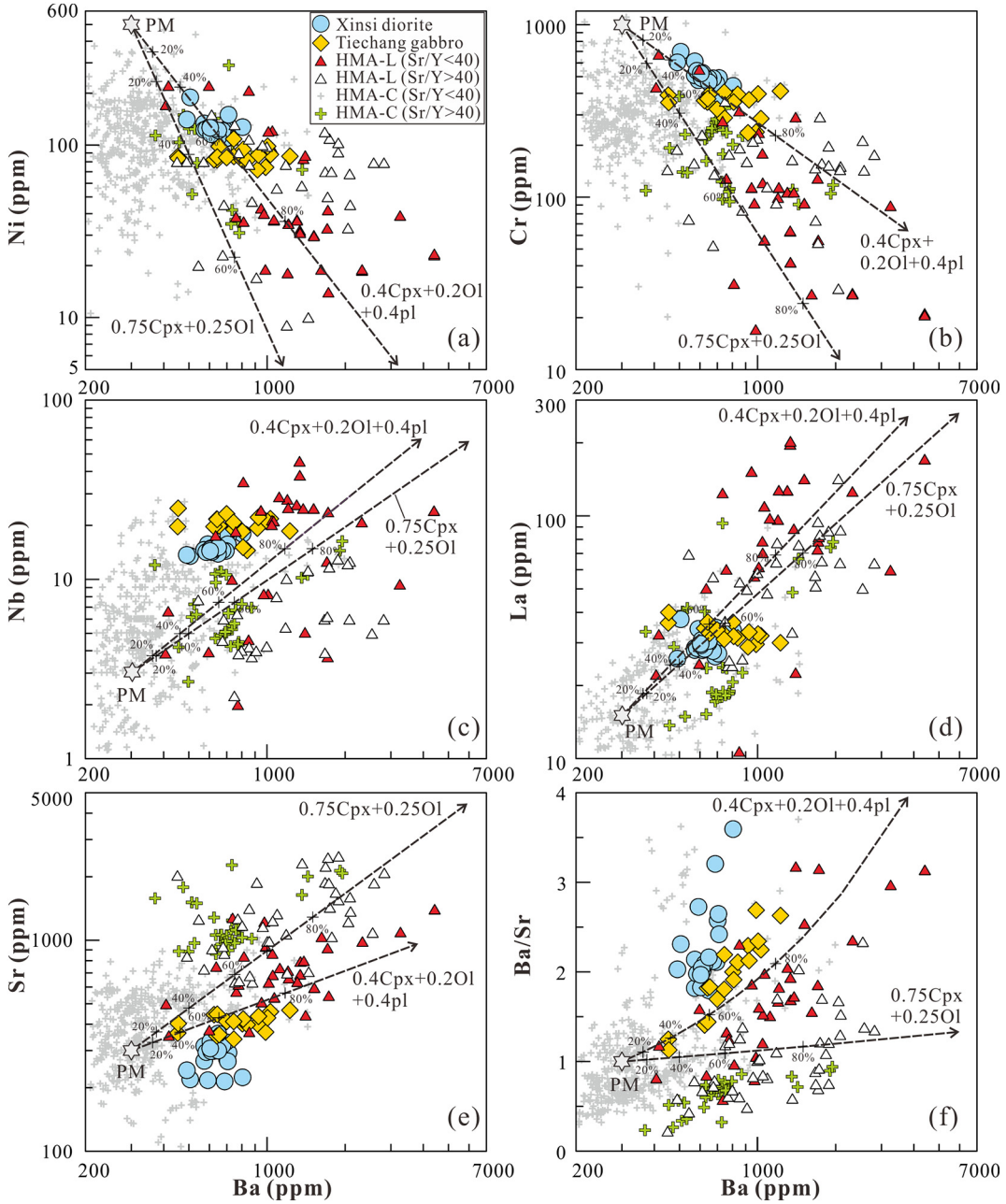

Fig. 12. Bivariate trace element plots of (a) Nb vs. Ba; (b) La vs. Ba; (c) Ni vs. Ba; (d) Cr vs. Ba; (e) Sr vs. Ba; (f) Ba/Sr vs. Ba for the Xinsi diorite and Tiechang gabbro, with the Cenozoic and Late Archean high-Mg andesitic rocks. Data sources of the Cenozoic and Late Archean high-Mg andesitic rocks (HMA-C and HMA-L, respectively) are same as Fig. 4. Fractional crystallization trends are calculated with partition coefficients from Beattie (1994), Bougault and Hekinian (1974), Dunn and Sen (1994), Hart and Dunn (1993) and Villemant et al. (1981). Abbreviations: PM = primary melt; Ol = olivine; Cpx = clinopyroxene; Pl = plagioclase.

Yogodzinski et al., 1995). The circum-Pacific high-Mg adakites show high Sr/Y (>40) ratios with high Ba and Sr contents (Figs. 4 and 10), and are thought to originate from slab-derived adakitic melts hybridized with the mantle wedge peridotite (Kay, 1978). The circum-Pacific low Sr/Y (<40) high-Mg andesites contain higher HREE (Fig. 5a) and lower Ba and Sr contents than the high-Mg adakites (Figs. 4 and 10), which is proposed to derive from a mantle source metasomatized by melts/fluids from subducted slab at shallow depths without involvement of garnet (e.g., Tatsumi, 2006). The Late Archean high-Mg andesitic rocks all have elevated Ba and Sr contents, resembling the circum-Pacific high-Mg adakites (Fig. 4), which have commonly been explained as partial melting of enriched mantle sources with inputs of TTG or adakitic melts from subducted slabs (e.g., Shirey and Hanson, 1984; Stern et al., 1989). Indeed, some Late Archean high-Mg andesitic rocks contain low HREE and Y contents and show high Sr/Y (>40) and La/Yb (Figs. 5 and 10), similar to the Cenozoic high-Mg adakites (Fig. 10). This is consistent with the involvement of TTG/adakitic melts in their mantle source (Heilimo et al., 2010; Lobach-Zhuchenko et al., 2008; Steenfelt et al., 2005; Stern et al., 1989). However, the Late Archean low Sr/Y high-Mg andesitic rocks show much higher HREE and Y contents and lower Sr/Y ratios (<40) than the adakites (Figs. 5 and 10), excluding the involvement of abundant garnet in their petrogenesis (Laurent et al., 2014).

The Xinsi diorites and Tiechang gabbros all evolved from low Ba—Sr parental melts and have high Ba, Nb and La contents through significant fractionation of Mg-rich minerals at normal crustal depths (Fig. 11), which are similar to the Late Archean high-Mg andesitic rocks except for slightly lower Sr (Figs. 4 and 10). The relatively low Sr contents of

the Xinsi diorite and Tiechang gabbro samples would be result of plagioclase fractionation (Fig. 11a and b), as evidenced by their negative Eu anomalies (Fig. 5). Therefore, the Xinsi diorites and Tiechang gabbros, as the Late Archean low Sr/Y high-Mg andesitic rocks, all have high HREE and Y contents and low Sr/Y ratios (Figs. 5 and 10), indicating absence of adakitic features (e.g., high Sr and Sr/Y > 40) for the melt input into their mantle sources. This demonstrates that the subducted slabs may have been melted at relatively low pressures without involving abundant garnet (e.g., Tatsumi, 2006).

Late Archean high-Mg andesitic rocks mostly have Mg# values lower than 0.65 (Martin et al., 2010) and tend to show lower MgO, Cr and Ni contents than Cenozoic high-Mg andesites (Fig. 4), indicating that they should have undergone fractional crystallization of Mg-rich minerals (i.e., olivine, pyroxenes and/or amphibole). It is noteworthy that the Late Archean high-Mg andesitic rocks with different Sr/Y ratios show distinct compositional trends (Fig. 12). The high Sr/Y (>40) high-Mg andesitic rocks show poor correlations between Ba and Cr, and between Ba and Ni (Fig. 12a and b), suggesting an insignificant contribution from mafic mineral fractionation to their high Ba and Sr abundances. In contrast, the Ba content of the low Sr/Y (<40) high-Mg andesitic rocks negatively correlate with Ni and Cr (Fig. 12a and b), which is consistent with the Ba enrichment trend due to the fractionation of Mg-rich minerals (i.e., olivine and pyroxene), as indicated by the Xinsi diorites and Tiechang gabbros. Other incompatible elements, such as Sr, Nb and La, all positively correlate with Ba (Fig. 12), denoting the progressive enrichment of these elements in the residual melts as a result of Mg-rich minerals fractionation. In comparison to the high Sr/Y high-Mg andesitic rocks, the low Sr/Y high-Mg andesitic rocks show negative Eu anomalies (Fig. 5), suggesting the involvement of plagioclase fractionation during their petrogenesis. The separation of plagioclase from magma can fractionate between Sr and Ba, as explicated by the Xinsi diorites and Tiechang gabbros (Fig. 11a and b). This process is also reflected by the low Sr/Y high-Mg andesitic rocks, which tend to show higher Ba/Sr ratios as Ba content increases (Fig. 12f). Since the Late Archean low Sr/Y high-Mg andesitic rocks with high Ni and Cr content have lower Sr and Ba content than those with low Ni and Cr (Fig. 12), we suggest that they might also evolve from low Ba and Sr parental melts similar to those of the Xinsi diorite and Tiechang gabbro. Thus, the Late Archean low Sr/Y high-Mg andesitic rocks may also derive from the partial melting of a mantle source with input of slab melts generated at shallow depths (e.g., <40 km). High Ba and Sr content of these low Sr/Y high-Mg andesitic rocks may be the result of crustal magmatic differentiation.

High-Mg andesitic rocks with variable Sr/Y ratios are present from the Late Archean to the Cenozoic and are thought to be associated with subduction (Tatsumi, 2006). The co-occurrence of high-Mg andesitic rocks and TTG during the Late Archean (3.0 to 2.5 Ga) in most cratons has been invoked as important evidence for the onset of modern subduction at the end of the Archean on Earth (e.g., Laurent et al., 2014). A prominent difference between Archean and modern subduction is that slab melting might have been more prevalent during the Late Archean because of higher mantle temperatures (Moyen and Martin, 2012). This can explain why the Late Archean high-Mg andesitic rocks generally have high La/Yb ratios, similar to the Xinsi diorites and Tiechang gabbros. In modern subduction zones, slab melting occurs predominantly at depths within the garnet stability field (i.e., >40 km) with the generation of adakites (Defant and Drummond, 1990), and the mantle wedge is mainly metasomatized by fluids from subducted slab at shallow depths (<40 km), which is evidenced by the highly variable Ba/La ratios in Cenozoic low Sr/Y high-Mg andesites (Fig. 10a). However, during the Late Archean, a hotter Earth would have resulted in higher geothermal gradients and subsequently more intense melting of subducted slab (Moyen and Martin, 2012). Accordingly, slab melting would take place at shallower depths (e.g., <40 km; Moyen and Martin, 2012), with the generation of low Ba and Sr and low Sr/Y melts. The partial melting of mantle sources with input of such melts can explain the formation of the low Sr/Y high-Mg andesitic rocks. The low Sr/Y and high Sr/Y high-Mg andesitic rocks in Middle to Late Archean were developed simultaneously, as exemplified by the 3.0 Ga Qeqertaussaq high Sr/Y diorite and Disko Bugt low Sr/Y diorite (Sr/Y ratios of ~76.2 and ~14.9, respectively; Garde, 1997; Steenfelt et al., 2005) in West Greenland and the 2.74–2.68 Ga high-Mg andesitic rocks from the Baltic Shield (Sr/Y = 9.48–530; Heilimo et al., 2010). The co-occurrence of low Sr/Y and high Sr/Y high-Mg andesitic rocks in Middle to Late Archean may record the intense melting of subducted slab at different depths under the hotter regime associated with the initiation of subduction on Earth.

6. Conclusions

The Xinsi diorites and Tiechang gabbros were derived from the partial melting of an enriched mantle source that had been refertilized during ancient subduction events. The parental melts have high La/Yb and low Ba/La ratios. The low Sr/Y high-Mg andesitic rocks are primarily low in Ba and Sr and could have high Ba and Sr contents through crustal magmatic differentiation instead of inputs of TTG or adakitic melts in the mantle source. Fractional crystallization plays an important role in the petrogenesis of high-Mg andesitic rocks.

Supplementary data to this article can be found online at https://doi.org/10.1016/j.lithos.2021.106069.

Declaration of Competing Interest

The authors declare that they have no known competing financial interests or personal relationships that could have appeared to influence the work reported in this paper.

The authors declare the following financial interests/personal relationships which may be considered as potential competing interests:

Acknowledgements

We thank L. Zhang, S.L. Sun, J.L. Ma and X.L. Tu for analytical assistance. We are grateful for the constructive comments from Qing Qian and R. H. Smithies, which significantly helped us to improve the quality of this paper. This study was financially supported by the National Natural Science Foundation of China (NSFC Projects U1701641, 41902056, 41625007, 41890812). This is contribution No. IS-2985 from GIGCAS.

References

Adam, J., Green, T., 2006. Trace element partitioning between mica- and amphibole-bearing garnet lherzolite and hydrous basanitic melt: 1. Experimental results and the investigation of controls on partitioning behavior. Contrib. Mineral. Petrol. 152 (1), 1–17.

Bea, F., 1996. Residence of REE, Y, Th and U in granites and crustal protoliths: Implications for the chemistry of crustal melts. J. Petrol. 37, 521–552.

Beattie, P., 1994. Systematics and energetics of trace-element partitioning between olivine and silicate melts: Implications for the nature of mineral/melt partitioning. Chem. Geol. 117, 57–71. https://doi.org/10.1016/0009–2541(94)90121–X.

Bougault, H., Hekinian, R., 1974. Rift valley in the Atlantic Ocean near 36°50'N: petrology and geochemistry of basalt rocks. Earth Planet. Sci. Lett. 24 (2), 249–261. https://doi.org/10.1016/0012–821X(74)90103–4.

Chauvel, C., Marini, J.C., Plank, T., Ludden, J.N., 2009. Hf-Nd input flux in the Izu-Mariana subduction zone and recycling of subducted material in the mantle. Geochem. Geophys. Geosyst. 10 (1). https://doi.org/10.1029/2008GC002101.

Defant, M.J., Drummond, M.S., 1990. Derivation of some modern arc magmas by melting of young subducted lithosphere. Nature 347, 662–665.

Dunn, T., Sen, C., 1994. Mineral/matrix partition-coefficients for ortho-pyroxene, plagioclase, and olivine in basaltic to andesitic systems - a combined analytical and experimental-study. Geochim. Cosmochim. Acta 58 (2), 717–733. https://doi.org/10.1016/0016–7037(94)90501–0.

Foster, M.D., 1960. Interpretation of composition of trioctahedral micas. U. S. Geol. Surv. Prof. Pap. 354B, 1–49.

Garde, A.A., 1997. Accretion and evolution of an Archaean High-Grade Grey Gneiss-Amphibolite Complex: The Fiskefjord Area, Southern West Greenland. Geol. Greenland Survey Bull. 177, 5–101.

Hart, S.R., Dunn, T., 1993. Experimental cpx/melt partitioning of 24 trace elements. Contrib. Mineral. Petrol. 113, 1–8.

Heilimo, E., Halla, J., Hölttä, P., 2010. Discrimination and origin of the sanukitoid series: geochemical constraints from the Neoarchean western Karelian Province (Finland). Lithos 115, 27–39.
Hermann, J., Rubatto, D., 2009. Accessory phase control on the trace element signature of sediment melts in subduction zones. Chem. Geol. 265, 512–526.
Hermann, J., Müntener, O., Günther, D., 2001. Differentiation of mafic magma in a continental crust-to-mantle transition zone. J. Petrol. 42, 189–206.
Hermann, J., Spandler, C., Hack, A., Korsakov, A.V., 2006. Aqueous fluids and hydrous melts in high-pressure and ultra-high pressure rocks: Implications for element transfer in subduction zones. Lithos 92, 399–417.
Herzberg, C., Condie, K., Korenaga, J., 2010. Thermal history of the Earth and its petrological expression. Earth Planet. Sci. Lett. 292 (1–2), 79–88.
Holland, T., Blundy, J., 1994. Non-ideal interactions in calcic amphiboles and their bearing on amphibole-plagioclase thermometry. Contrib. Mineral. Petrol. 116, 433–447.
Huang, D.L., Wang, X.L., Xia, X.P., Zhang, F.F., Wang, D., Sun, Z.M., Li, Y.J., Yang, Q., Du, D.H., Chen, X., 2020. Crustal anatexis recorded by zircon grains from early Paleozoic granitic rocks in Southeast China. Lithos 370–371, 105598.
Huang, X.L., Yu, Y., Li, J., Tong, L.X., Chen, L.L., 2013. Geochronology and petrogenesis of the early Paleozoic I-type granite in the Taishan area, South China: Middle-lower crustal melting during orogenic collapse. Lithos 177, 268–284.
Jochum, K.P., Weis, U., Schwager, B., Stoll, B., Wilson, S.A., Haug, G.H., Andreae, M.O., Enzweiler, J., 2016. Reference Values following ISO guidelines for frequently Requested Rock Reference Materials. Geostand. Geoanal. Res. 40 (3), 333–350.
Kay, R.W., 1978. Aleutian magnesian andesites: melts from subducted Pacific Ocean crust. J. Volcanol. Geotherm. Res. 4, 117–132.
Kessel, R., Schmidt, M.W., Ulmer, P., Pettke, T., 2005. Trace element signature of subduction-zone fluids, melts and supercritical liquids at 120–180 km depth. Nature 437, 724–727.
Kinzler, R.J., 1997. Melting of mantle peridotite at pressures approaching the spinel to garnet transition: Application to mid-ocean ridge basalt petrogenesis. J. Geophys. Res.-Solid Earth 102, 853–874.
Laurent, O., Martin, H., Moyen, J.F., Doucelance, R., 2014. The diversity and evolution of late-Archaean granitoids: evidence for the onset of "modern-style" plate tectonics between 3.0 and 2.5 Ga. Lithos 205, 208–235.
Leake, B.E., Woolley, A.R., Arps, C.E.S., Birch, W.D., Gilbert, M.C., Grice, J.D., Hawthrone, F.C., Kato, A., Kisch, H.J., Krivovischev, V.G., Linthout, K., Laird, J., Mandarino, J.A., Maresch, W.V., Nickel, E.H., Rock, N.M.S., Schumacher, J.C., Smith, D.C., Stephenson, N.C.N., Ungaretti, L., Whittaker, E.J.W., Youzhi, G., 1997. Nomenclature of amphiboles: Report of the subcommittee on amphiboles on the International Mineralogical Association, Commission on new minerals and mineral names. Am. Mineral. 82, 1019–1037.
Li, X.H., Li, Z.X., Wingate, M.T.D., Chung, S.L., Liu, Y., Lin, G.C., Li, W.X., 2006. Geochemistry of the 755Ma Mundine well dyke swarm, northwestern Australia: part of a Neoproterozoic mantle superplume beneath Rodinia? Precambrian Res. 146, 1–15.
Li, X.H., Liu, Y., Li, Q.L., Guo, C.H., Chamberlain, K.R., 2009. Precise determination of Phanerozoic zircon Pb/Pb age by multicollector SIMS without external standardization. Geochem. Geophys. Geosyst. 10, Q04010. https://doi.org/10.1029/2009GC002400.
Li, X.H., Long, W.G., Li, Q.L., Liu, Y., Zheng, Y.F., Yang, Y.H., Chamberlain, K.R., Wan, D.F., Guo, C.H., Wang, X.C., Tao, H., 2013a. Penglai zircon megacrysts: a potential new working reference material for microbeam determination of Hf-O Isotopes and U-Pb Age. Geostand. Geoanal. Res. 34 (2), 117–134.
Li, X.H., Tang, G.Q., Guo, B., Yang, Y.H., Hou, K.J., Hu, Z.C., Li, Q.L., Liu, Y., Li, W.X., 2013b. Qinghu zircon: a working reference for microbeam analysis of U-Pb age and Hf and O isotopes. Chin. Sci. Bull. 58, 4647–4654. https://doi.org/10.1007/s11434-013-5932-x.
Li, Z.X., Li, X.H., Wartho, J.A., Clark, C., Li, W.X., Zhang, C.L., Bao, C., 2010. Magmatic and metamorphic events during the early Paleozoic Wuyi-Yunkai Orogeny, southeastern South China: new age constraints and pressure-temperature conditions. Geol. Soc. Am. Bull. 122, 772–793.
Liu, S.F., Peng, S.B., Kusky, T., Polat, A., Han, Q.S., 2018. Origin and tectonic implications of an early Paleozoic (460–440 Ma) subduction-accretion shear zone in the northwestern Yunkai Domain, South China. Lithos 322, 104–128.
Lobach-Zhuchenko, S.B., Rollinson, H., Chekulaev, V.P., Savatenkov, V.M., Kovalenko, A.V., Martin, H., Guseva, N.S., Arestova, N.A., 2008. Petrology of late Archean, Highly Potassic, Sanukitoid Pluton from the Baltic Shield: insights into late Archean Mantle Metasomatism. J. Petrol. 49, 393–420.
Ludwig, K.R., 2003. Isoplot: a geochronological toolkit for Microsoft Excel. Berkeley Geochronol. Center Special Publication 4, 1–67.
Martin, H., 1987. Petrogenesis of Archaean trondhjemites, tonalites, and granodiorites from Eastern Finland: major and trace element geochemistry. J. Petrol. 28, 921–953.
Martin, H., Smithies, R.H., Rapp, R., Moyen, J.F., Champion, D., 2005. An overview of adakite, tonalite-trondhjemite-granodiorite (TTG), and sanukitoid: relationships and some implications for crustal evolution. Lithos 79 (1–2), 1–24.
Martin, H., Moyen, J.F., Rapp, R., 2010. The sanukitoid series: magmatism at the Archaean-Proterozoic transition. Earth and Environ. Sci. Transac. Royal Soc. Edinburgh 100, 15–33. https://doi.org/10.1017/s1755691009016121.
McCarthy, T.C., Patino Douce, A.E., 1998. Empirical calibration of the silica-Catschermak's-anorthite (SCAn) geobarometer. J. Metamorph. Geol. 16, 675–686.
McKenzie, D., O'Nions, R.K., 1991. Partial melt distributions from inversion of rare Earth element concentrations. J. Petrol. 32, 1021–1091.
Moore, G., Carmichael, I.S.E., 1998. The hydrous phase equilibria (to 3 kbar) of an andesite and basaltic andesite from western Mexico: constraints on water content and conditions of phenocryst growth. Contrib. Mineral. Petrol. 130, 304–319.
Moyen, J., Martin, H., 2012. Forty years of TTG research. Lithos 148, 312–336.
Moyen, J.F., Martin, H., Jayananda, M., Auvray, B., 2003. Late Archaean granites: a typology based on the Dharwar Craton (India). Precambrian Res. 127, 103–123.
Nebel, O., Capitanio, F.A., Moyen, J.F., Weinberg, R.F., Clos, F., Nebel-Jacobsen, Y.J., Cawood, P.A., 2018. When crust comes of age: on the chemical evolution of Archaean, felsic continental crust by crustal drip tectonics. Phil. Trans. R. Soc. A 376, 20180103. https://doi.org/10.1098/rsta.2018.0103.
Plank, T., Langmuir, C.H., 1998. The chemical composition of subducting sediment: implications for the crust and mantle. Chem. Geol. 145, 325–394.
Pouchou, J.L., Pichoir, F., 1991. Quantitative analysis of homogeneous or stratified microvolumes applying the model "PAP". In: Heinrich, K.F.J., Newbury, D.E. (Eds.), Electron Probe Quantification. Plenum Press, New York, pp. 31–75.
Qian, Q., Hermann, J., 2010. Formation of high-Mg diorites through assimilation of peridotite by monzodiorite magma at crustal depths. J. Petrol. 51, 1381–1416.
Qian, Q., Hermann, J., Wang, Y.L., Guo, J.H., Liu, F., Wang, L.J., 2015. Variations of clinopyroxene/melt element partitioning during assimilation of olivine/peridotite by low-Mg diorite magma. Chem. Geol. 419, 36–54.
Rapp, R.P., Shimizu, N., Norman, M.D., Applegate, G.S., 1999. Reaction between slab-derived melts and peridotite in the mantle wedge: experimental constraints at 3.8 GPa. Chem. Geol. 160, 335–356.
Rapp, R.P., Norman, M.D., Laporte, D., Yaxley, G.M., Martin, H., Foley, S.F., 2010. Continental formation in the Archean and chemical evolution of the cratonic lithosphere: Melt-rock reaction experiments at 3-4GPa and petrogenesis of Archean Mg-diorites. J. Petrol. 51 (6), 1237–1266.
Salters, V.J.M., Stracke, A., 2004. Composition of the depleted mantle. Geochem. Geophys. Geosyst. 5.
Schmidt, M.W., 1992. Amphibole composition in tonalite as a function of pressure: an experimental calibration of the Al-in-hornblende barometer. Contrib. Mineral. Petrol. 110, 304–310.
Shirey, S.B., Hanson, G.N., 1984. Mantle-derived Archaean monzodiorites and trachyandesites. Nature 310, 222–224.
Sláma, J., Košler, J., Condon, D.J., Crowley, J.L., Gerdes, A., Hanchar, J.M., Horstwood, M.S.A., Morris, G.A., Nasdala, L., Norberg, N., Schaltegger, U., Schoene, B., Tubrett, M.N., Whitehouse, M.J., 2008. Plešovice zircon-a new natural reference material for U-Pb and Hf isotopic microanalysis. Chem. Geol. 249, 1–35.
Smithies, R.H., Champion, D.C., 2000. The Archaean high-Mg diorite suite: links to tonalite-trondhjemite-granodiorite magmatism and implications for early Archaean crustal growth. J. Petrol. 41, 1653–1671.
Smithies, R.H., Champion, D.C., Sun, S.S., 2004. Evidence for early LREE-enriched mantle source regions: diverse magmas from the c. 3.0 Ga Mallina Basin, Pilbara Craton, NW Australia. J. Petrol. 45, 1515–1537.
Smithies, R.H., Champion, D.C., Van Kranendonk, M.J., Howard, H.M., Hickman, A.H., 2005. Modern style subduction processes in the Mesoarchaean: geochemical evidence from the 3.12 Ga Whundo intra-oceanic arc. Earth Planet. Sci. Lett. 231, 221–237.
Smithies, R.H., Lu, Y.J., Johnson, T.E., Kirkland, C.L., Cassidy, K.F., Champion, D.C., Mole, D.R., Zibra, I., Gessner, K., Sapkota, J., De Paoli, M.C., Poujol, M., 2019. No evidence for high-pressure melting of Earth's crust in the Archean. Nat. Commun. 10, 5559. https://doi.org/10.1038/s41467-019-13547-x.
Spandler, C., Mavrogenes, J., Hermann, J., 2007. Experimental constraints on element mobility from subducted sediments using high-P synthetic fluid/melt inclusions. Chem. Geol. 239, 228–249.
Steenfelt, A., Garde, A.A., Moyen, J.F., 2005. Mantle wedge involvement in the petrogenesis of Archaean grey gneisses in West Greenland. Lithos 79, 207–228.
Stern, R.A., Hanson, G.N., Shirey, S.B., 1989. Petrogenenesis of mantle-derived, LILE enriched Archean monzodiorites and trachyandesites (sanukitoids) in southwestern Superior Province. Can. J. Earth Sci. 26, 1688–1712.
Stevenson, R., Henry, P., Gariépy, C., 1999. Assimilation-fractional crystallization origin of Archean sanukitoid suites: Western Superior Province, Canada. Precambrian Res. 96, 83–99.
Sun, S.S., McDonough, W.F., 1989. Chemical and isotopic systematics of oceanic basalts: Implication for mantle composition and process. In: Sauders, A.D., Norry, M.J. (Eds.), Magmatism in the Ocean Basins. Geological Society Special Publications vol. 42, pp. 313–345.
Tatsumi, Y., 2006. High-Mg Andesites in the Setouchi Volcanic Belt, Southwestern Japan: Analogy to Archean Magmatism and Continental Crust Formation? Annu. Rev. Earth Planet. Sci. 34, 467–499.
Tatsumi, Y., Ishizaka, K., 1982. Origin of high-magnesium andesite in the Setouchhi volcanic belt, Southwest Japan, 1. Petrographical and chemical characteristics. Earth Planet. Sci. Lett. 60, 293–304.
Ulmer, P., Kaegi, R., Müntener, O., 2018. Experimentally Derived Intermediate to Silica-rich Arc Magmas by Fractional and Equilibrium Crystallization at 1.0 GPa: an Evaluation of phase Relationships, Compositions, liquid Lines of Descent and Oxygen Fugacity. J. Petrol. 59 (1), 11–58.
Villemant, B., Jaffrezic, H., Joron, J.L., Treuil, M., 1981. Distribution Coefficients of Major and Trace-elements - Fractional Crystallization in the Alkali Basalt Series of Chaine-Des-Puys (Massif Central, France). Geochim. Cosmochim. Acta 45 (11), 1997–2016. https://doi.org/10.1016/0016–7037(81)90055–7.
Wang, Y.J., Zhang, A.M., Fan, W.M., Zhao, G.C., Zhang, G.W., Zhang, F.F., Zhang, Y.Z., Li, S.Z., 2011. Kwangsian crustal anatexis within the eastern South China Block: geochemical, zircon U-Pb geochronological and Hf isotopic fingerprints from the gneissoid granites of Wugong and Wuyi-Yunkai Domains. Lithos 127, 239–260.
Wang, Y.J., Zhang, A.M., Fan, W.M., Zhang, Y.H., Zhang, Y.Z., 2013. Origin of paleosubduction-modified mantle for Silurian gabbro in the Cathaysia Block: geochronological and geochemical evidence. Lithos 160–161, 37–54.
Wei, G.J., Liang, X.R., Li, X.H., Liu, Y., 2002. Precise measurement of Sr isotopic compositions of liquid and solid base using (LA) MC-ICP-MS. Geochimica 31, 295–305 (in Chinese with English abstract).

Wells, P.R.A., 1977. Pyroxene thermometry in simple and complex systems. Contrib. Mineral. Petrol. 62, 129–139.

Woodhead, J.D., Hergt, J.M., Davidson, J.P., Eggins, S.M., 2001. Hafnium isotope evidence for 'conservative' element mobility during subduction zone processes. Earth Planet. Sci. Lett. 192, 331–346.

Yogodzinski, G.M., Kay, R.W., Volynets, O.N., Koloskov, A.V., Kay, S.M., 1995. Magnesian andesite in the western Aleutian Komandorsky region: Implications for slab melting and processes in the mantle wedge. Geol. Soc. Am. Bull. 107, 505–519.

Yu, Y., Huang, X.L., He, P.L., Li, J., 2016. I-type granitoids associated with the early Paleozoic intracontinental orogenic collapse along pre-existing block boundary in South China. Lithos 248–251, 353–365.

Yu, Y., Huang, X.L., Sun, M., He, P.L., 2018. Petrogenesis of early Paleozoic granitoids and associated xenoliths in the Baoxu and Enping plutons, South China: Implications for the evolution of the Wuyi-Yunkai intracontinental orogeny. J. Asian Earth Sci. 156, 59–74.

Yu, Y., Huang, X.L., Sun, M., Yuan, C., 2020. Missing Sr-Nd isotopic decoupling in subduction zone: Decoding the multi-stage dehydration and melting of subducted slab in the Chinese Altai. Lithos 362–363, 105465.

Zhang, L., Ren, Z.Y., Xia, X.P., Li, J., Zhang, Z.F., 2015b. IsotopeMaker: a Matlab program for isotopic data reduction. Int. J. Mass Spectrom. 392, 118–124.

Zhang, L., Ren, Z.Y., Xia, X.P., Yang, Q., Hong, L.B., Wu, D., 2019. In situ determination of trace elements in melt inclusions using laser ablation-inductively coupled plasma-sector field-mass spectrometry. Rapid Commun. Mass Spectrom. 33, 361–370.

Zhang, Q., Jiang, Y.H., Wang, G.C., Liu, Z., Ni, C.Y., Qing, L., 2015a. Origin of Silurian gabbros and I-type granites in Central Fujian, SE China: Implications for the evolution of the early Paleozoic orogen of South China. Lithos 216–217, 285–297.

Zhong, Y.F., Wang, L.J., Zhao, J.H., Liu, L., Ma, C.Q., Zheng, J.P., Zhang, Z.J., Luo, B.J., 2016. Partial melting of an ancient sub-continental lithospheric mantle in the early Paleozoic intracontinental regime and its contribution to petrogenesis of the coeval peraluminous granites in South China. Lithos 264, 224–238.